Magnetohydrodynamics in liquid metal interfacial flows

Ming-Jiu Ni[a, c]
[a] School of Engineering Sciences, University of Chinese Academy of Sciences
No.1 Yanqihu East Rd, Huairou District, Beijing, PR China, 101408
[c] State Key Lab of Nonlinear Mechanics, Institute of Mechanics, Chinese Academy of Sciences
No.15 Beisihuanxi Road, Beijing, PR China, 100190
mjni@ucas.ac.cn

Juan-Cheng Yang [b, 1]
[b] State Key Laboratory for Strength and Vibration of Mechanical Structures, School of Aerospace, Xi'an Jiaotong University
No.28 Xianning West Road, Xi'an, Shaanxi 710049, P.R. China
yangjc@xjtu.edu.cn

Jie Zhang[b, 2]
[b] State Key Laboratory for Strength and Vibration of Mechanical Structures, School of Aerospace, Xi'an Jiaotong University
No.28 Xianning West Road, Xi'an, Shaanxi 710049, P.R. China
j-zhang@xjtu.edu.cn

ABSTRACT

Liquid metal interfacial flows occur in the fields of nuclear fusion and electromagnetic metallurgy. Due to the electrically conductive characteristics of the liquid metal, the presence of magnetic fields in these application scenarios has significant impacts on the interfacial flow behaviors. Then typical interfacial flows under the influence of magnetic fields, such as the free surface liquid metal flow, the liquid metal droplet impacting problems, and the bubble motion in liquid metal, are discussed in the present review. We comprehensively illustrate the flow characteristics of free surface liquid metal flow, the spreading of liquid metal droplets impacting onto solid or liquid surfaces, outcomes of collisions between metal droplets, and bubble dynamics in liquid metal, under the influence of magnetic fields along different

[1] Address all correspondence related to the content of experiments to this author.
[2] Address all correspondence related to the content of simulations to this author.

directions. Meanwhile, we briefly review the current concepts of liquid metal free surface flow Plasma Facing Components (PFCs) in fusion reactors and finally make a summary for the open questions related to the fundamental research and industrial applications of interfacial flow magnetohydrodynamics in the future.

1 INTRODUCTION

Interfacial flow refers to the motion of at least two kinds of fluid with differing physical properties, such as the boundary between immiscible fluids (e.g., oil and water), the surface between a liquid and a gas, or the interface between a liquid and a solid substrate. These flows exist diversely in nature and industry, including free surface film flows, droplet impact dynamics, bubble motion in liquids, and particle motion in fluid environments [1,2]. In this review, we only focus on the liquid metal interfacial flow with gas serving as a secondary fluid phase, a scenario commonly encountered in nuclear fusion reactors and electrometallurgy. Specifically, we consider the effects of magnetic fields on these interactions, namely, the magnetohydrodynamic (MHD)effects.

In the Tokamak system, the plasma-facing components (PFCs) are important parts to contain and control the plasma, manage extreme thermal loads, protect against erosion, handle impurities, and assist in neutron shielding. Despite extensive testing of various solid materials for PFCs, an ideal solution has yet to be discovered. Given the benefits of flow liquid metal in engineering applications, scientists introduced the innovative concept of covering the solid PFCs with a layer of free surface liquid metal flow, known as liquid metal PFCs, in fusion reactors to address these challenges [3,4]. Nevertheless, there are still lots of issues that need to be solved due to the existence of

the strong magnetic field in the Tokamak system. Achieving a continuously flowing liquid lithium film characterized by stable surfaces and uniform thickness presents a significant challenge, primarily due to the influence of the MHD effect. Specifically, when the liquid metal film flow intersects a magnetic field (B_0) the resultant Lorentz force alters the force balance, leading to a flow behavior that is markedly different from that observed without a magnetic field.

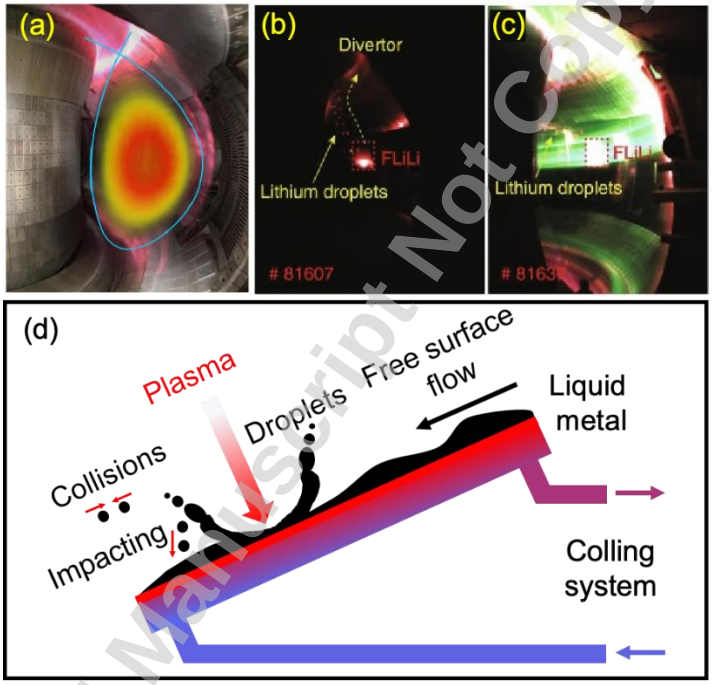

Fig.1. (a) Photo of plasma in the EAST device. Droplets are generated when the plasma is without (b) and with (c) NBI heating [5]. (CC BY 4.0) (d) Schematic diagram of the possible liquid metal flow when the PFCs work in the Tokamak device, i.e., free surface flow, droplets impact.

Hu et al. [6] carried out plenty of experiments on a continuously flowing liquid lithium (FLiLi) limiter in the Experimental Advanced Superconducting Tokamak (EAST). Their results indicated that achieving complete coverage of solid PFCs with lithium-free

surface flow was challenging, and the interaction with plasma led to the formation of numerous droplets on the lithium surface (Fig.1(b) and (c)). The formation of these droplets was closely associated with the magnetic field, the stability of the film flow, and the plasma characteristics. On the one hand, the instability of the film flow surface facilitates the generation of droplets; on the other hand, these droplets, upon impacting the liquid film surface, introduce further perturbations to the flow, complicating the stability of the film. At the same time, the sputtered droplet motion will generate some possible phenomena, such as mutual collisions and impacts on unwetted solid surfaces of PFCs. Figure 1(d) shows the typical interfacial flows that may happen during the liquid metal PFCs working in the Tokamak environment, i.e., the liquid metal free surface flow, and the droplets impacting. To ensure a stable free surface liquid metal flow in the design of PFCs, a comprehensive understanding of liquid metal interfacial flow phenomena is essential. Up to now, numerous researchers have carried out relevant work and contributed to the discovery and understanding of these phenomena, which is the first main objective of this review.

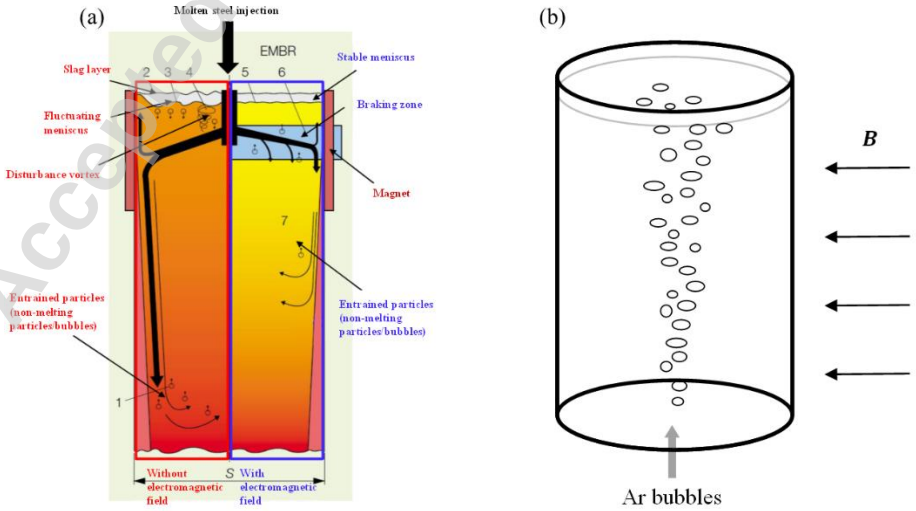

Fig. 2. Schematic view for bubble plume applied in metallurgical engineering and fusion reactors, where magnetic fields are at present. (a) Bubble plume in metallurgic processing. (b) Configuration of the bubble column used in experiments and numerical simulations [7]. Copyright by the Cambridge University Press (2007). Reproduced with permission.

Bubble-driven flows are also common phenomena in metallurgical processes and nuclear fusion devices, where bubbles are introduced into molten metals to enhance mixing and heat transfer [7-15]. In metallurgical engineering, magnetic fields are employed to control bubble motion in a contactless manner, thereby improving the uniformity of liquid metal properties and the overall quality of final products. Figure 2(a) gives a schematic view of the bubbly flows in metallurgical processing, where the gas bubbles are injected to enhance mixing in the melt and to support chemical reactions. In fusion reactors, bubbles are particularly useful in mitigating turbulence suppression caused by MHD effects, thereby improving energy transfer efficiency [3]. While the integration of bubbles and magnetic fields has significantly advanced these applications (see Figure 2(b) for a sketch of the experimental setup [7]), the precise effects of MHD on bubble interactions and distributions remain inadequately understood, necessitating further in-depth research. The rising behavior of single bubbles in transparent fluids, such as in water, has been extensively studied, leading to well-characterized motion patterns like zigzagging, spiral, and even chaos trajectories. However, liquid metals pose additional complexities due to their opacity, high density, and electrical conductivity, which make direct observation and experimentation challenging [16, 9]. In the absence

of a magnetic field, high Reynolds number (Re, defined as the ratio of the inertial force of the fluid to the viscous force) conditions in liquid metal lead to path instabilities of a rising bubble, with the trajectory exhibiting a zigzag or spiral path due to wake instabilities and vortex shedding [17-20]. At lower Re, bubbles tend to follow more stable, straight paths. Besides, the wake structures are observed to be more complex in liquid metal than in water, owing to the much higher rising Re and the much stronger shape deformation in liquid metal. In the presence of magnetic fields, the magnetic fields introduce Lorentz forces that can modulate the surrounding liquid flow, thereby affecting the bubble's trajectory, velocity, shape evolution, and void distribution. Recent studies have provided a certain level of understanding of these phenomena, which is another main topic of this review.

2 GOVERNING EQUATIONS AND NUMERICAL SCHEMES

2.1 Flow computations

The incompressible free surface flows exposed to external magnetic fields (MFs) are governed by some physical principles, which are, respectively, the conservation of mass equation, the momentum equation, and the Maxwell equation. The governing mass and momentum equations are given by

$$\rho\left(\frac{\partial \boldsymbol{u}}{\partial t}+\boldsymbol{u}\cdot\nabla\boldsymbol{u}\right)=-\nabla p+\nabla\cdot[\mu(\nabla\mathbf{u}+\nabla\mathbf{u}^{T})]+\boldsymbol{F}_{s}+\boldsymbol{F}_{l}+\boldsymbol{S}, \tag{1}$$

$$\nabla\cdot\boldsymbol{u}=0, \tag{2}$$

where $\boldsymbol{u}$ is the fluid's velocity, ρ and μ denote the density and dynamic viscosity of the immiscible fluids. The two sources in terms of $\boldsymbol{F_l}$ and $\boldsymbol{F_s}$ are the Lorentz force and the surface tension force, respectively. The former is calculated as $\boldsymbol{F}_{l}=\boldsymbol{J}\times\boldsymbol{B}$, where $\boldsymbol{J}$

129 denotes the induced current density and $\boldsymbol{B}$ is the MF. Note that for the free surface
130 flows concerned in the present review, the magnetic Reynolds number $\mathrm{Re_m} =$
131 $\mu_m \sigma_e L U \ll 1$ in liquid metal is very low ($\sim 10^{-3}$), with μ_m denoting the magnetic
132 permeability, σ_e the electrical conductivity, and U the characteristic fluid velocity.
133 Hence, the induced MFs by the fluid motion are much smaller than the applied MFs, and
134 therefore a quasi-static approximation can be used [21], leading to $B = B_0$, where B_0 is
135 the external magnetic field. In this regard, the electric potential method can then be
136 used to compute the current densities, expressed by Ohm's law as below:

$$J = \sigma_e(-\nabla\varphi + \boldsymbol{u} \times \boldsymbol{B}), \tag{3}$$

137 where φ is the induced electric potential. Then due to the conservative property
138 of the charge, the divergence-free condition of $\nabla \cdot \boldsymbol{J} = 0$ should be maintained during
139 computations that an additional electric potential Poisson equation requires to be
140 solved, given as

$$\nabla \cdot (\sigma_e \nabla\varphi) = \nabla \cdot (\sigma_e \boldsymbol{u} \times \boldsymbol{B}). \tag{4}$$

141 Consequently, the combination of Eqs. (3) and (4) leads to the solution of the
142 current densities $\boldsymbol{J}$, and then the Lorentz forces in Eq. (1) are obtained. On the other
143 hand, the surface tension force, in the absence of a tangential Marangoni stress, has the
144 expression of $\boldsymbol{F}_s = \sigma\kappa\delta_s\boldsymbol{n}$, where σ and κ are the surface tension coefficient and the
145 local curvature of the interface, respectively, while $\boldsymbol{n}$ is the normal direction of the
146 interface and δ_s the Dirac distribution function. At last, $\boldsymbol{S}$ appeared at the right-hand
147 side of Eq. (1) is the remaining source term, which always stands for the gravity $\rho\boldsymbol{g}$ in
148 interfacial flows.

To solve the equations governing the fluid flow, i.e. Eq. (1), the essential step is to ensure the divergence-free condition of the velocity in terms of Eq. (2). Upon on this, some numerical methods have been proposed to decouple the solution of the pressure field from the momentum equation, and the most popular approach is the fractional-step method [22,23]. Then this type of methodology has been widely applied to solve the incompressible magnetohydrodynamics [19,20,24-29]. We take the numerical method proposed by Zhang et al. [19] for instance, the discretized forms of Eq. (1) are given as

$$\rho_c^{n+\frac{1}{2}}\left(\frac{\boldsymbol{u}^* - \boldsymbol{u}^n}{\Delta t} + \boldsymbol{u}^{n+\frac{1}{2}} \cdot \nabla \boldsymbol{u}^{n+\frac{1}{2}}\right)_c = \nabla_c \cdot \left[\mu_f^{n+\frac{1}{2}} (\nabla \boldsymbol{u} + \nabla \boldsymbol{u}^T)^*\right] + (\boldsymbol{J} \times \boldsymbol{B})_c^{n+\frac{1}{2}} + \left[(\sigma \kappa \delta_s \boldsymbol{n})^{n-\frac{1}{2}} - \nabla p^n\right]_{f \to c}, \tag{5}$$

$$\boldsymbol{u}_c^{**} = \boldsymbol{u}_c^* - \frac{\Delta t}{\rho_c^{n+\frac{1}{2}}}\left[(\sigma \kappa \delta_s \boldsymbol{n})^{n-\frac{1}{2}} - \nabla p^n\right]_{f \to c}, \tag{6}$$

$$\boldsymbol{u}_f^{n+1} = \boldsymbol{u}_{c \to f}^{**} + \frac{\Delta t}{\rho_f^{n+\frac{1}{2}}}\left[(\sigma \kappa \delta_s \boldsymbol{n})^{n+\frac{1}{2}} - \nabla p^{n+1}\right]_f \tag{7}$$

where the velocity and the pressure fields are solved at time step $(n+1)$. We see that in this discretization process, based on the principle of the balanced-force model [30], the discretization of the surface tension force $\boldsymbol{F}_s$ should always stay with the pressure gradient ∇p, to minimize the spurious flow in the vicinity of the interface. Besides, the subscripts c and f indicate where the variables are stored, corresponding to the "center" and the "face" of the discretized grids, respectively, while the symbol $c \to$

$f(f \rightarrow c)$ means a second-order interpolation scheme from cell center (face) to cell face (center) by applying a simply arithmetic average. In the methodology proposed by Zhang et al. [19], all the variables, i.e. the velocity, the pressure, and other scalar fields, are located at the center of the grids, while the pressure gradient (∇p) and the surface tension force ($\sigma\kappa\delta_s \boldsymbol{n}$) are calculated on the grid faces. Then a projection method is applied on Eq. (8) to enhance the divergence-free condition of the flow, that is:

$$\nabla_c \cdot \left[\frac{\Delta t}{\rho^{n+\frac{1}{2}}} \left((\sigma\kappa\delta_s \boldsymbol{n})^{n+\frac{1}{2}} - \nabla p^{n+1} \right) \right]_f = \nabla_c \cdot \boldsymbol{u}_f^{n+1} - \nabla_c \cdot \boldsymbol{u}_{c\rightarrow f}^{**} \tag{8}$$

where $\nabla_c \cdot \boldsymbol{u}_f^{n+1}$ is zero. Because $(\sigma\kappa\delta_s \boldsymbol{n})^{n+\frac{1}{2}}$ and $\boldsymbol{u}_{c\rightarrow f}^{**}$ are already obtained in solving Eq. (7) and (8), therefore (p^{n+1}) could be computed through applying an iterative approach on Eq. (8). After that, the grid face velocity of $\boldsymbol{u}_f^{n+1}$ is updated by substituting (p^{n+1}) into Eq. (8), and the grid center velocity of $\boldsymbol{u}_c^{n+1}$ is interpolated through

$$\boldsymbol{u}_c^{n+1} = \boldsymbol{u}_c^{**} + \frac{\Delta t}{\rho_c^{n+\frac{1}{2}}} \left[(\sigma\kappa\delta_s \mathbf{n})^{n+\frac{1}{2}} - \nabla p^{n+1} \right]_{f\rightarrow c} \tag{9}$$

Additionally, in the presence of external magnetic fields, a consistent and conservative scheme [24,26] is now usually employed to compute the electric currents and Lorentz forces, in terms of Eqs. (3) and (4). Because of this, the progression of the numerical solution on the electromagnetic part from time level n to level $n+1$ is given below:

$$\nabla_c \cdot (\sigma_e \nabla\varphi)_f^{n+\frac{1}{2}} = \nabla_c \cdot \left(\sigma_e (\boldsymbol{u} \times \boldsymbol{B}) \right)_f^{n+\frac{1}{2}} \tag{10}$$

$$\boldsymbol{J}_f^{n+\frac{1}{2}} = \left(\sigma_e(-\nabla\varphi + \boldsymbol{u}\times\boldsymbol{B})\right)_f^{n+\frac{1}{2}} \tag{11}$$

$$\boldsymbol{F}_l^{n+\frac{1}{2}} = (\boldsymbol{J}\times\mathbf{B})_{f\to c}^{n+\frac{1}{2}} \tag{12}$$

Then, the remaining technique that requires clarification is the discretization of the surface tension term $\boldsymbol{F}_s = \sigma\kappa\delta_s\boldsymbol{n}$. As will be demonstrated later, accurately estimating $\boldsymbol{F}_s$ proves to be a non-trivial task in numerical simulations.

2.2 Interface tracking and surface tension computation

The most intuitive way to update the position of the free surface is to describe the shape of the interface by distributing a finite number of material particles on the interface. The positions of these particles (and thus the shape of the interface) could then be updated using

$$\frac{d\boldsymbol{x}_I^k}{dt} = \boldsymbol{u}, \tag{13}$$

where $\boldsymbol{x}_I^k$ denotes the position of the interface in the *k*-th grid, and this equation complies with the Lagrangian system. This class of methods is often called front-tracking or marker methods [31], while they can be implemented and solved with high accuracy. However, to ensure an appropriate description of the interface, marker particles need to be redistributed periodically along the interface, which complicates practical implementations. Upon on this methodology, Schwarz and Fröhlich [32] developed an immersed boundary method to model the single bubble rising under the influence of a vertical magnetic field, while the surface of the bubble is described using a set of

Lagrangian marker points interconnected by a triangular mesh. Then the motion of a single bubble is obtained by solving its linear and angular momentum equation.

Alternatively, the other way to track the interface is to define the interface position implicitly, i.e., through an arbitrary function such that $\mathcal{F}(\boldsymbol{x})_I = 0$, and rather than discretizing the interface itself, one can then choose to discretize the implicit function $\mathcal{F}$. With this regard, $\mathcal{F}$ must also evolve in time to reflect the evolution of the interface, yielding that

$$\frac{\partial \mathcal{F}}{\partial t} + \boldsymbol{u} \cdot \nabla \mathcal{F} = 0, \tag{14}$$

and this means $\mathcal{F}$ is simply advected by the flow as an ordinary tracer. This approach always falls into an Euler framework, and the most popular methods include the level-set (LS) [33,34] and the volume of fluid (VOF) [35,36], the former defines $\mathcal{F}$ as the signed distance to the interface while the later defines $\mathcal{F}$ as the volume fraction the continuous or disperse phase. LS does degrade the accuracy with which the position of the interface $\boldsymbol{x}_I$ is estimated because it is thus necessary to periodically re-initialize $\mathcal{F}$, and this in turn can cause large errors in mass conservation. The LS method has been implemented in the in-house code of HIMAG [37], which was developed at UCLA for the modeling of the free surface MHD flows. In contrast, the VOF method can conserve the mass of the fluid better, and the implementation of the numerical algorithm, for the discretization of Eq. (14), is also simple. In particular, a split-direction advection scheme, i.e. using the one-dimensional scheme for alternative propagation, is always applied to update the volume fraction $\mathcal{F}$ to next time step $n + \frac{1}{2}$. During this split-direction process, the interface can be reconstructed either using a geometrical scheme [36] or an algebraic scheme [38], to

maintain the sharpness of the immiscible interface. The application of the VOF method can be also found in the MHD research community [20,39,40]. After obtaining $\mathcal{F}^{n+\frac{1}{2}}$, a physical property $\phi(\text{i.e.}, \rho, \mu \text{ and } \sigma_e)$ at a given position of the fluid domain is evaluated by linear interpolation as $\phi^{n+\frac{1}{2}} = \mathcal{F}^{n+\frac{1}{2}}\phi_1 + (1-\mathcal{F})^{n+\frac{1}{2}}\phi_2$, where 1 and 2 are the properties of the two phases.

Now we turn to the discretization of the surface tension force $\boldsymbol{F}_s = \sigma\kappa\delta_s\boldsymbol{n}$, which is closely related to the interface position defined by $\mathcal{F}$. There are two different methodologies to compute this term. On the one hand, volumetric formulations are based on a numerical approximation of the surface Dirac function, which allows a direct evaluation of the volumetric force, while most methods belong to this category independently of the way the interface is represented. For instance, for the widely used Continuum Surface Force (CSF) method developed by Brackbill et al. [41], the interface is represented through the volume fraction field $\mathcal{F}$ and one simply sets $\boldsymbol{F}_s = \sigma\kappa\delta_s\boldsymbol{n} = \sigma\kappa\nabla\mathcal{F}$, which makes the characteristic interface thickness to be non-zero but spread over several grids. In contrast, the other kind of method maintains the sharpness of the interface when computing the surface tension, and it is usually associated with LS interface representations known as the Ghost Fluid Method [42,43]. Such a method treats the surface tension as the corresponding jump condition in the discretization of the pressure gradient operator, i.e., $p^{-}_{i-\frac{1}{2}} = p_i \pm (\sigma\kappa)_{i-\frac{1}{2}}$ and thus leads to a sharp interface representation, in contrast with the other methods. Both of these two types of numerical methods have been applied in modeling the surface tension force of the

interfacial MHD flows, respectively, by Zhang et al. [39,40] and Jin et al. [20], and they both show good agreements compared to the experimental studies.

3 FREE SURFACE LIQUID METAL FLOW

Film flow and open channel flow are two typical free surface flows. Open channel flow is common in rivers and canals where the liquid is deep, while film flow is common in sheets of rainwater on glass. This review focuses mainly on the liquid metal free surface flow used in liquid metal diverters in nuclear fusion reactors, where the magnetic field is present. A summary of the effects of magnetic field magnitude, direction, flow rate, and wall conductivity on the characteristics of film flow is provided.

3.1 Stability of liquid metal free surface flow

Stability is a crucial aspect in the study of free surface flow. It can help us understand and predict flow behavior, essential for optimizing various industrial applications. Kapitza et al. [44] are pioneers in investigating the wave dynamics on thin liquid layers. By adopting the long-wave expansion, Benjamin [45] studied the origin of film flow instability. The long-wave hydrodynamic instability mainly stems from the flow direction component of gravity, inertia, and hydrostatic pressure [46].

The introduction of MFs gives rise to the generation of an additional electromagnetic force acting within the free surface flow, which in turn exerts an influence on the stability of the free surface flow. Hesieh [47] firstly investigated the stability of liquid films influenced by magnetic fields using the long-wave approximation. Results indicated that magnetic fields have a stabilizing effect on long-wave

disturbances. Similarly, Ladikov [48]and Shen et al. [49] arrived at the same conclusion. Rai [50] and Mukhopadhyay et al. [51] adopted the asymptotic approximation of the linear stability equation based on the long wave assumption and the weakly nonlinear analysis to study the stability of free surface flow within the influence of magnetic field, respectively. Subsequently, the Galerkin method [52] or the Chebyshev collocation method [53] was employed to solve the Orr-Sommerfeld (OS) eigenvalue problem. Generally, a neutral stability curve can be obtained in the $(\mathrm{K}, \mathrm{Re})$ plane, where K is the wave number in the flow direction. The region inside the curve indicates instability, while the area outside the curve signifies stability, thereby allowing for the determination of parameters such as the critical Reynolds number for instability. Gotoh [54] adopted the neutral stability curve (Fig. 3) to determine the parameter range of Re and N^*, corresponding to the stability and instability of free shear flow under the influence of a vertical magnetic field, here N^* is defined as $\mathrm{Ha}^2/\mathrm{Re}^2$.

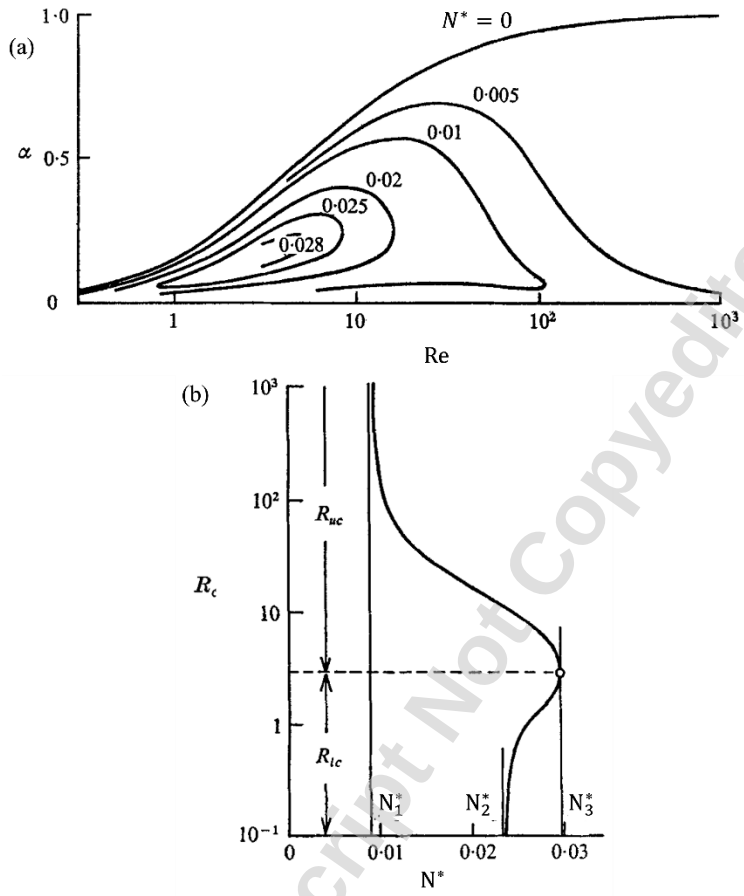

Fig. 3. Results from Gotoh [54]. (a) Neutral stability curves corresponding to different magnetic field parameters N^* under two-dimensional disturbance, (b) Relationship between critical Reynolds number Re and magnetic field parameter N^* under two-dimensional disturbance. Copyright by the Cambridge University Press (1971). Reproduced with permission.

Moreover, the direction of the MFs exerts a significant influence on the stability of the free surface. When the generated Lorentz force points towards the interior of the fluid, it will result in surface wave instability, as demonstrated by Murty [55]. When the Lorentz force is in an upward direction and exceeds the gravitational force, Rayleigh-Taylor instability will occur on the free surface, as discussed by Shercliff [56].

Considering the cases that the magnetic Prandtl number P_m, $P_m = \nu/\eta$, is small, which is the ratio of kinematic viscosity ν to magnetic diffusivity η, the magnetic field has a stabilizing effect on the flow and is less dependent on P_m [57,47]. Different magnetic field components have different stabilizing effects on liquid film flow [49].

In the presence of a transverse non-uniform magnetic field, the amplitude of surface disturbances along the flow direction is significantly enhanced, while the propagation speed of these disturbances is reduced [58-60]. Moreover, under the vertical magnetic field, the hard mode of free surface flow behaves similarly to the unstable mode of channel Hartmann flow at low-magnetic-Prandtl-number regime ($P_m \ll 10^{-4}$,), and it is less affected by P_m. However, the soft mode is more sensitive to changes in P_m[52]. In the inductionless limit $P_m > 0$, the critical Re of the soft mode increases exponentially with Ha, while when P_m is mall but non-zero, the Lorentz force causes the critical Re to sub-linearly increase with Ha for insulating walls or decrease for perfectly conductive walls. Weak nonlinear analysis shows that under the influence of a vertical magnetic field, the flowing liquid film has both supercritical instability and subcritical instability. Meanwhile, with the increase of Hartmann number, subcritical and explosive unstable zones are enlarged and shrank respectively [51]. In the supercritical stable region and subcritical unstable region, the threshold amplitude decreases and increases respectively with the increase of Hartmann number M (Fig. 4), here M is the same as Ha. In addition, the effect of the electric field on the flow stability depends on its direction [51,61]. In the subcritical region, the wave velocity and amplitude threshold of the nonlinear wave increase with the increase of Ha, and in the

supercritical region, the wave velocity and amplitude threshold of the nonlinear wave decrease with the increase of Ha. Cheng et al. [62] analyzed the rupture of micropolar films under the effect of MFs using the long wave approximation. The findings indicated that as the initial disturbance diminished, the film breakage time extended. Furthermore, the micropolarity and magnetic fields exhibited a significant impact on the film flow on the horizontal plate.

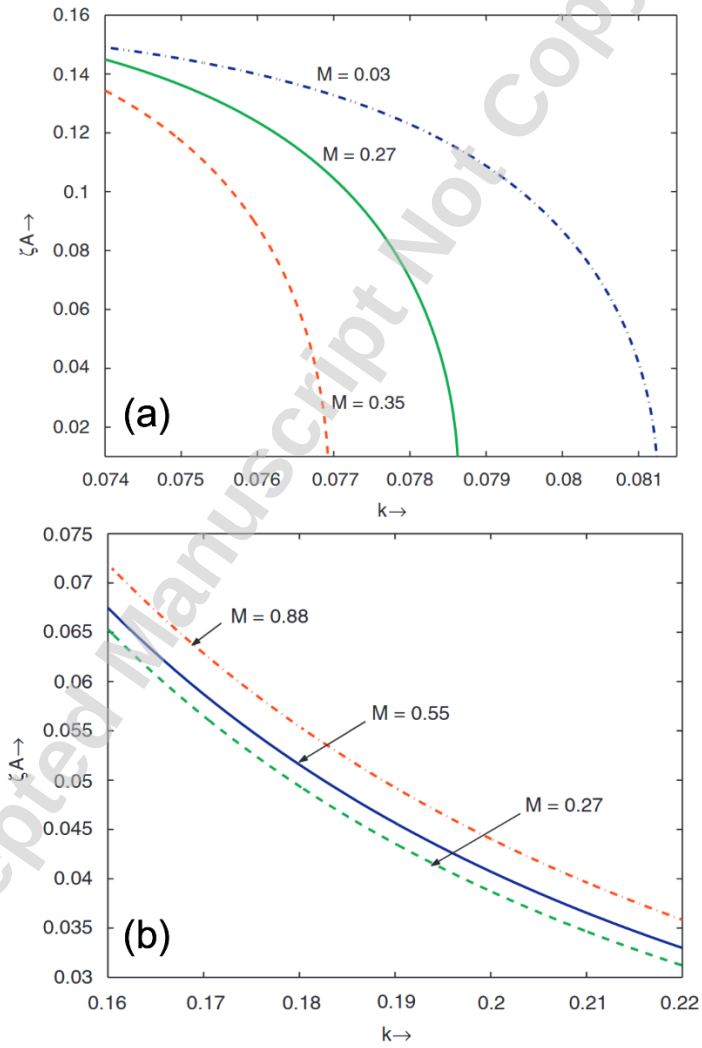

Fig. 4. (a) Threshold amplitude in the supercritical region for different values of Hartmann number, (b) Threshold amplitude in the subcritical region for different values

of Hartmann number [51]. (Noting that M is the same as Ha). Copyright by the Elsevier (2008). Reproduced with permission.

Lunz et al. [63] analyzed the stability of the flowing liquid film on the conical surface under the influence of the toroidal magnetic field. The toroidal magnetic field serves to stabilize the flow, although the Hartmann layer is absent for the conical surface. When the surface tension can be ignored, the flow stability is related to parameters such as magnetic field intensity, local Re, liquid film thickness, and inclination angle. The local critical Reynolds number increases sharply with the increase of the magnetic field. According to the results from stability analysis, the critical Reynolds number can be expressed as a function of other parameters (Fig. 5), so one can adjust the relevant parameters to obtain the largest possible critical Reynolds number to make the flow more stable.

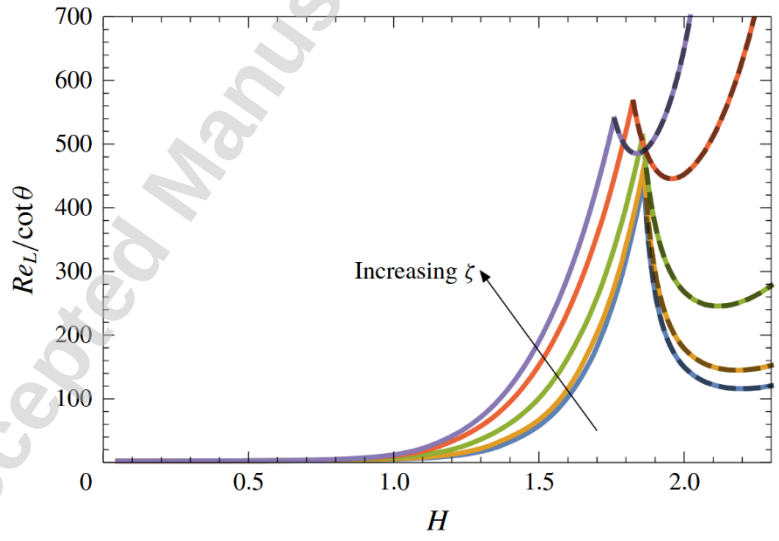

Fig. 5. Numerically computed critical local Reynolds number $\mathrm{Re_L}/\cot\theta$ as a function of *H*, for ζ [63]. Copyright by the Cambridge University Press (2019). Reproduced with permission.

In addition to velocity disturbances and electromagnetic disturbances, factors such as thermal gradients generated by local heating or cooling drive thermocapillary flows [64]. The shape of the substrate [65], and gas flow or plasma [66] also affect interface stabilities. Feedback control systems [67] or open-loop control systems [68] can be designed to stabilize the instability of the free interface by selecting the system's material, customizing the system geometry, controlling the forcing amplitude, or using the thermodynamic principles. For a uniformly heated descending film, there are two thermocapillary instability modes proposed by Goussis and Kelly [69]: (1) short-wave thermocapillary instability caused by the interaction between the basic temperature field and the perturbed velocity field, also known as the P-mode; (2) long-wave thermocapillary instability due to surface temperature changes caused by free surface deformation, also known as S-mode. Usually, the thermocapillary instability will cause the well-known Maragonni effect. That is, when there is a wave on the surface of the liquid film, the temperature of the free surface close to the heated wall is high, and the temperature of the liquid film far from the wall is low. For most liquids, their surface tension decreases with increasing temperature, and the fluid will move from areas with low surface tension to areas with high surface tension, further aggravating the surface deformation of the liquid film. Nield [70] first discovered that the critical Marangoni number for the onset of Marangoni convection increases with increasing magnetic field strength. However, for a deformable free surface, the magnetic field cannot stabilize all disturbances [71]. Subsequently, Hasilmn et al. [72] calculated the critical parameter space for the occurrence of oscillatory Marangoni convection.

353

354 3.2 Morphology of surface waves

355 Surface waves can provide a clear indication of flow stability, as their behavior
356 directly reflects the underlying dynamics of the fluid. Therefore, many researchers have
357 engaged in studies related to this topic.

358 In the middle of 20 century, Alpher et al. [73] provided a detailed review of the
359 surface waves in shallow mercury flows. Without a magnetic field, surface waves in
360 mercury follow classical gravity wave dynamics, with propagation speed determined by
361 $gh_0^{1/2}$. Waves experience minimal attenuation, allowing disturbances to propagate
362 further. The prominent capillary waves form sharp "fish-line" patterns due to surface
363 tension. Hydraulic jumps in mercury flows behave similarly to those observed in classical
364 shallow-water flows. Murav'ev [74] revisited the "shallow water" approximation for
365 analyzing wave regimes on the free surface of liquid metal films. He found that the wave
366 behavior is primarily influenced by gravitational forces, slope angles, and the properties
367 of the liquid metal (e.g., viscosity and density). The corresponding equations derived for
368 wave dynamics align with classical hydrodynamic models, such as the Froude number
369 (Fr, $\mathrm{Fr} = U/\sqrt{gh}$), which determines whether the flow regime is "fast" or "quiet".
370 Morley et al. [75-78] systematically investigated the liquid metal film flow from
371 theoretical, numerical simulation, and experiments. Their results also proved that the
372 liquid metal film flows exhibit primarily hydrodynamic behavior. The stability and
373 behavior of these waves depend on factors like Reynolds (Re, $\mathrm{Re} = Ul/\nu$) number,
374 Weber (We, $\mathrm{We} = \rho U^2 l/\sigma$) number, and Fr. When the flow is unstable, surface waves,

a common feature in such flows, can arise due to instabilities caused by inclinations, high flow rates, or external disturbances caused by rough gates or nozzle misalignments. Ying et al. [79] observed the irregular, three-dimensional (3D) turbulent wave structures that result from hydrodynamic instabilities.

From the hydrodynamic aspect, the flow state of film flow can be divided into three regimes: smooth laminar flow, wavy laminar flow, and turbulent flow, respectively [80]. These three regimes can be divided by Ka and Re in figure 6. The Kapitza number Ka is expressed as the ratio of surface tension to inertial force, which is equal to $\sigma/(\rho(g\sin\beta)^{1/3}\nu^{4.3})$. For liquid flowing on steep or vertical walls, smooth laminar flow only occurs at very low flow rates. Free surface waves can be subdivided into gravity type, capillary type, and gravity-capillary type, with gravity or surface tension as the main restoring forces, respectively. Gravity waves appear around $\mathrm{Fr} = 1{\sim}2$, while capillary waves appear around $\mathrm{We} = 1$. The corresponding wave frequency of gravity waves, capillary waves, and gravity-capillary waves can be expressed as $\omega^2 = gk\tanh(kh)$, $\omega^2 = \gamma k^3$, and $\omega^2 = (gk + \gamma k^3)\tanh(kh)$ respectively, where ω is the frequency of the wave, k is the wave number, g is gravity acceleration, h is the thickness of liquid, and $\gamma = \sigma/\rho$ is the ratio of surface tension σ coefficient to density of liquid. The crossover between the gravity waves and capillary waves occurs for the wavelength $\lambda_{gc} = 2\pi\sqrt{\sigma/(\rho g)}$ [81]. It is important to note that the presence of waves does not necessarily mean that the flow is turbulent [80].

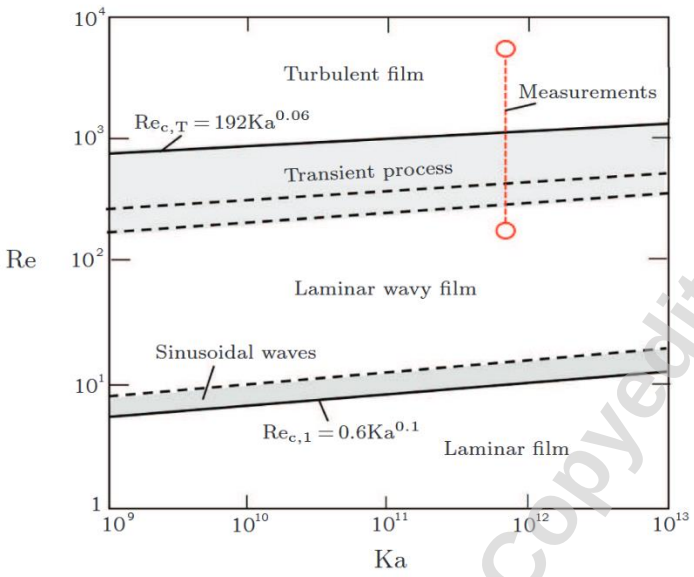

Fig. 6. Typical flow regimes in Ka − Re space, the red dashed line presents the results measured by Vieweg et al. [82] under the influence of the magnetic field. (CC BY 4.0)

However, interactions between surface waves, such as inelastic collisions, can make the waves more complex [83]. For example, in a random wave field, non-resonant interactions can generate bound waves that deviate from the liner dispersion relation [84]. In addition, intermittency occurs when the wave height increments follow a Gaussian distribution on large scales but deviate significantly from the Gaussian distribution on small scales [85]. The non-equilibrium statistical mechanics of such random nonlinear waves can be studied by using wave turbulence theory [86]. Similar to classical turbulence theory, there is energy transfer caused by wave interaction in wave turbulence, and the state of the wave system can be determined by conservation quantities such as energy flux. Through dimensional analysis, the Kolmogorov-Zakharov Spectrum of different wave systems can be obtained to reveal the distribution and

transfer mechanisms of energy [87]. For a general capillary wave system, $S_\omega^c \sim P^{1/2}(\sigma/\rho)^{1/6}\omega^{-17/6}$, while for a general capillary wave system, $S_\omega^g \sim P^{1/3} g\omega^{-4}$. Here S_ω^c and S_ω^g are the power spectral density of capillary wave elevation and gravity wave elevation, respectively, and P is the energy flux. Currently, there is no analytical solution for the Kolmogorov-Zakharov spectrum of gravity capillary wave turbulence, as the dispersion relation is not a pure power law [81]. Instead, it comprises two distinct power laws within the power spectral density of wave height, representing gravity waves and capillary waves, respectively.

Considering the liquid metal free surface flow with side walls, the surface waves containing small-scale fluctuations and vorticity can easily cause the liquid metal to pinch towards the center of the channel, leaving bare zones near the sidewalls. Such behavior is particularly evident when the liquid metal does not wet the substrate well. As shown in Fig. 7, at low Re, due to the wetting problem, the GaInSn forms an unstable liquid column flow, exhibiting random surface striations [88]. As the Reynolds number increases, the flow becomes unstable and moves to the sides of the channel, and after reaching the critical Reynolds number, the flow begins to spread.

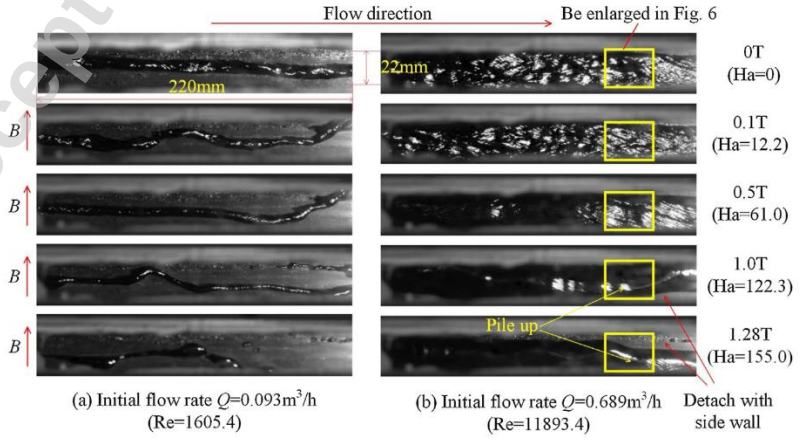

Fig. 7. Different flow patterns of liquid metal with the increase of Ha, (a) $\mathrm{Re} = 1605.4$, (b) $\mathrm{Re} = 11893.4$ [88]. Copyright by the Elsevier (2016). Reproduced with permission.

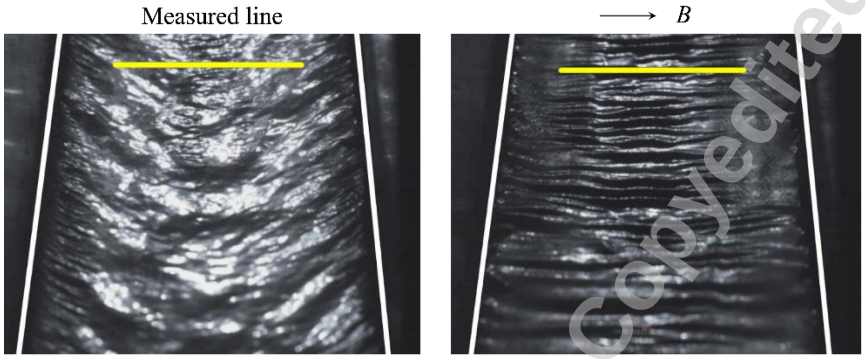

(a) Re = 4661, Ha = 0 (b) Re = 4661, Ha = 120

Fig. 8. The surface topology observed by a high-speed camera when the inclination angle of the test section is 5° without (a) and with (b) the effect of the magnetic field [90].

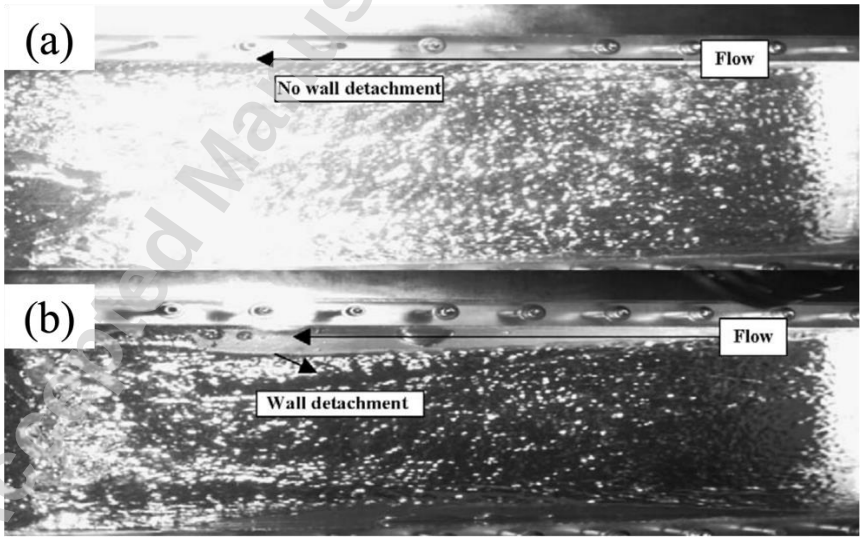

Fig. 9. The surface waves of liquid metal film flow. (a) Flow state of the film flow with a vertical magnetic field, (b) Flow state of the film flow without magnetic field [90]. Copyright by the Elsevier (2006). Reproduced with permission.

438 According to the governing equation in Sec. 2, conductive liquid metal flowing in
439 a magnetic field will produce electromagnetic induction, and the resulting MHD effect
440 makes the free surface flow of liquid metal different from ordinary free surface flow.
441 Moreover, the MHD effect is anisotropic, the velocity component in the same direction
442 as the magnetic field will not be suppressed, and the same is true for the vorticity. Ying
443 et al. [91] found that the magnetic field significantly alters the characteristics of surface
444 waves in the liquid metal flow. As shown in Fig.9, in high magnetic field strength regions,
445 a distinct departure from the ordinary hydrodynamic turbulence observed in low-field
446 regions [90]. This indicates a strong influence of the magnetic field on wave formation
447 and propagation, transitioning the wave behavior from typical hydrodynamic patterns
448 to a more structured, possibly stabilized, state at higher field strengths. The exact
449 nature of this transition and the underlying mechanisms require further investigation,
450 but the clear difference in wave structure highlights the substantial impact of the
451 magnetic field on the free surface dynamics. In the experiments from Yang et al. [88],
452 they also found that the MHD effect has an important influence on the change of the
453 flow patterns. When Re is small, the magnetic field induces a flow perturbation that
454 makes the fluid oscillate, and the flow becomes discontinuous with the increase of
455 Hartmann number Ha, which is equal to $Bl(\sigma_e/\rho\nu)^{1/2}$. Therefore, it is necessary to
456 change the wettability between the substrate and the liquid metal. Common
457 approaches include coating the substrate, printing surface microstructures on the
458 substrate [92], or using special structures such as metal mesh [65].

Regarding the changes in surface topologies, Yang et al. [89] observed the transition of three-dimensional surface waves to quasi-two-dimensional (Q2D) surface waves with wave propagated perpendicular to the direction of magnetic lines, as shown in Fig. 8(b), indicating that the magnetic field suppresses waves with wave vectors parallel to it. Rhoads [93] observed gravity capillary waves on the surface of a flowing film and explained the effect of the magnetic field on the wave amplitude from an energy perspective. In the absence of artificially created waves, the fluctuations at the free surface may be caused by velocity disturbance. That is a localized rise in the fluid, followed by a change in direction and fall due to continuity as it approaches the free surface, resulting in localized vorticity. The restoring forces that prevent this change include electromagnetic forces, surface tension, and gravity. By omitting the influence of surface tension, Rhoads [93] suggested that the change in free surface amplitude should overcome the sum of gravity and electromagnetic force, $(g + \alpha B^2) < h >$, where α is a dimensionless parameter which is equal to $\sigma_e B^2/\rho\omega$ and varies with the nature of the surface disturbance [94]. Therefore, the average energy per unit mass supplied by the velocity perturbation to the surface wave is equal to $< \tilde{u}^2 >/2$. By making the two energies equal, they obtained an equation (Eq. 15) to predict the surface amplitude.

$$< h > = \frac{< \tilde{u}^2 >/2}{(g + \alpha B^2)} \tag{15}$$

From ref. [93], it can be seen that the surface amplitude predicted by Eq. 15 agrees well with the experimental data. Among them, the electromagnetic term is caused by $|\boldsymbol{J} \times \boldsymbol{B}|$, and $\boldsymbol{J} = \sigma_e(\boldsymbol{E} + \boldsymbol{u} \times \boldsymbol{B})$. Therefore, when there is an angle between the vorticity field or the velocity field and the magnetic field, the corresponding

electromagnetic term is non-zero, and the electromagnetic force suppresses the surface disturbance. The wave component propagating along the flow direction corresponds to a local vorticity in the same direction as the transverse magnetic field. Therefore, the damping of the magnetic field on the stream direction wave (down-stream) is much weaker than that of the wave vector propagating along the transverse direction (cross-stream). Although the mechanism of magnetic field suppression is the same, compared with the transverse magnetic field, a vertical magnetic field will suppress surface fluctuations in all directions because the plane where the wave vector lies is always perpendicular to the magnetic field. As the vertical magnetic field increases, the surface wave components in the streamwise direction and the transverse direction decrease with a consistent trend. In addition, the relationship between the wave amplitude and the magnetic field is relatively independent of the liquid depth and flow rate, as evidenced by [93]. Normally, the energy of gravity capillary waves on a free surface is transferred from large scales to small scales according to a certain power law. However, according to Rhoads' experimental results [93], the magnetic field not only suppresses the amplitude of the waves, that is, the energy of the waves, but also changes the speed of the transfer of the wave energy and even suppresses the wave energy to the noise level.

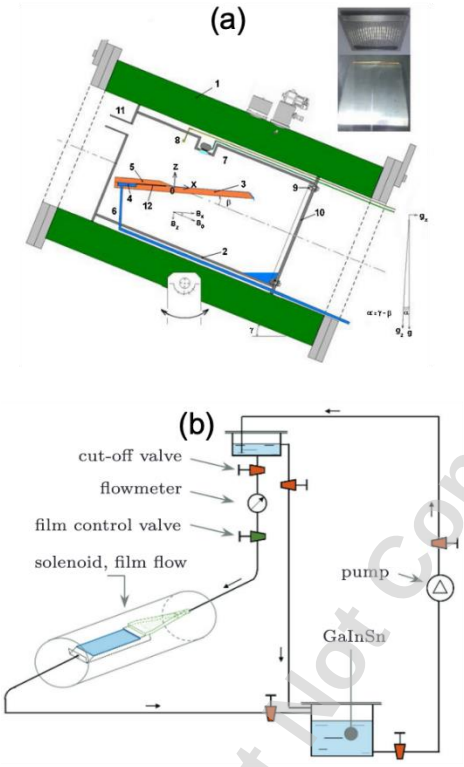

Fig. 10. Experimental systems to study the free surface flow under the influence of streamwise magnetic field. Schematic of experimental systems established by Platacis et al. [95] (a) (Copyright by the Elsevier (2014). Reproduced with permission.) and by Vieweg et al. [82] (b). (CC BY 4.0)

Concerning the influence of streamwise magnetic field on liquid metal surface waves, experimental results remain notably limited. Figure 10 shows two typical experimental systems. In the experimental system established by Platacis et al. [95] (Figure 10(a)), the magnetic field and the flow direction are not perfectly parallel but are instead slightly misaligned at an angle, causing effects in both the vertical and parallel flow directions. The induced current generated by the magnetic field in the vertical component interacts with the streamwise magnetic field component to change the pressure distribution [95]. Meanwhile, the Lorentz force in the vertical direction will also

disturb the flow. When only considering the streamwise magnetic field, Vieweg et al. [82] observed obvious changes in the flow state under the effect of the magnetic field, the red dashed line displayed in Fig. 6. This suggests the existence of an additional axis perpendicular to the $\mathrm{Ka}-\mathrm{Re}$ space and related to Stuart number $\mathrm{N}=\mathrm{Ha}^2/\mathrm{Re}$.

By designing a special system with controllable waves on the surface of liquid metal, Ji et al. [94] studied the effect of a horizontal magnetic field (magnetic field direction is parallel to wave vector) on surface waves and their dispersion relations. They predicted the wave-damping rate caused by the magnetic field through linear theory, which is given by

$$\exp\left[-\frac{B_{0x}^2\omega k_r}{2\rho_e(\rho\omega^2+2\sigma k_r^3)}\Delta x\right] \tag{16}$$

where k_r is the real part of the wave number, and B_{0x} is the external streamwise magnetic field, and ρ_e is electrical resistivity. The greater the magnetic field strength, the faster the wave is damped. However, the observed value is much larger than the theoretical prediction, because the prediction only considers the MHD effect during wave propagation. Although the magnetic field does not change the dispersion relation of the wave vector perpendicular to it [96], it affects the dispersion relation of parallel waves. Ji et al. [94] summarized the influence of the electromagnetic field on the dispersion relation as Eq. 17, where j_y is the cross-channel current density, B_x is the streamwise magnetic field, and $K^2=k^2(1-i\sigma_e B_x^2/\rho\omega)$. The imaginary part shows that the surface wave is damped due to the Joule dissipation from the streamwise magnetic field component. Moreover, liquid metal oxides will change the surface

tension coefficient so that the dispersion relation curve of the surface wave deviates from the standard curve.

$$\rho\omega^2 = \left(\rho g + k^2\sigma + j_y B_x\right)\frac{k^2}{K}\tanh(Kh) \tag{17}$$

3.3 Thickness of liquid metal free surface flow

The thickness of liquid metal free surface flow, which can be influenced by the magnetic field, flow velocity, and inclination angle of the substrate, is also an important parameter. In the smooth laminar flow region without the influence of a magnetic field, there was a 1/3 scaling law (Eq. 18) between the Nusselt film thickness N_T and the Reynolds number [80], which can be derived from Navier-Stokes equations. According to the empirical equations, the scale in the turbulent region varied between 1/2 and 2/3.

$$N_T = h(g\sin\beta/\nu^2)^{1/3}\left(\frac{\rho-\rho_c}{\rho}\right)^{1/3} = (3\mathrm{Re})^{1/3} \tag{18}$$

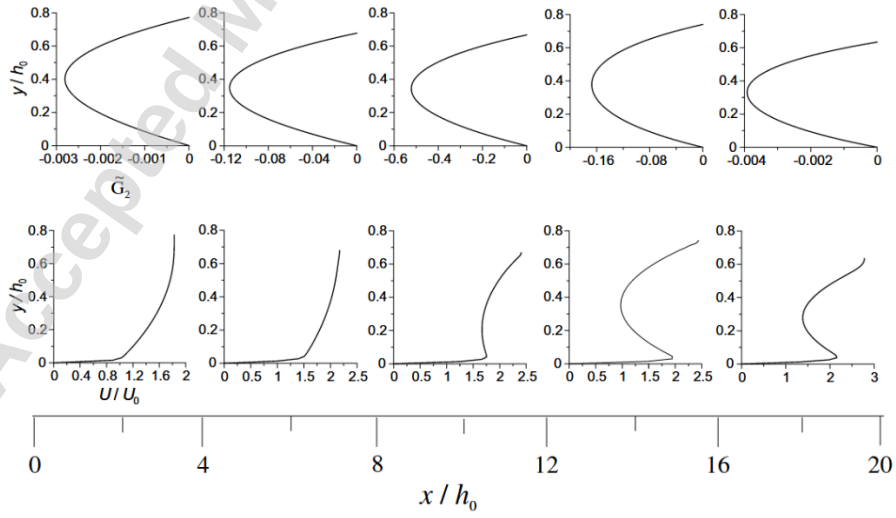

Fig. 11. Downstream variations of the velocity profile (lower) and adverse pressure gradient (upper) [97]. Copyright by the Elsevier (2005). Reproduced with permission.

Under the influence of the transverse magnetic field, the Lorentz force acts as a resistance, reducing the flow velocity and even forming an adverse pressure gradient in the core flow, causing the vertical distribution of the velocity to change from a parabolic shape to an "M" shape, similar to the velocity distribution of a conductive rectangular duct under the influence of a transverse magnetic field (Fig. 11). Therefore, the thickness of the liquid film will also change. Compared with the case without the magnetic field, the thickness of the film increases, even accumulating at the entrance of the test section [89,98,99]. Since the upstream and downstream of the test section were located at the entrance and exit of the magnetic field, respectively, they were within the gradient magnetic field range. Sun et al. [98] measured the distribution of the liquid film thickness along the flow direction and found that the slope of the flow surface height was moderate in the two regions, so the accumulation of liquid metal was mainly caused by the magnetic field strength rather than the magnetic field gradient.

In addition, when Ha is small, the thickening effect of the magnetic field on the thickness of the liquid film is not obvious. Then, the thickness increases linearly with the increase of Ha, but the slope of the linear relationship is affected by Re and the inclination angle β. Yang et al. [89] investigated the effects of each of the above three parameters on the liquid film thickness by controlling the variables and obtained an empirical correlation, $\delta_{en} \sin\beta \sim 0.012\mathrm{N}$ (the solid line in Fig. 12), where δ_{en} is the

565 relative film thickening, $\delta_{en} = (h_{av} - h_0)/h_0$, and h_{av} and h_0 are the average thickness
566 and average thickness without the magnetic field, and Stuart number N. It can be seen
567 in Fig. 12 that there is a critical Stuart number $\mathrm{N_{cr}}$ when N is greater than $\mathrm{N_{cr}}$, the MHD
568 drag force plays a dominant role in the changes in liquid film thickness and flow velocity.
569 Similar to transverse magnetic fields, vertical magnetic fields exert a force opposite to
570 the main flow direction, suppressing the flow and thickening the liquid film. Moreover,
571 the position of the Hartmann layer varies with different magnetic field directions.

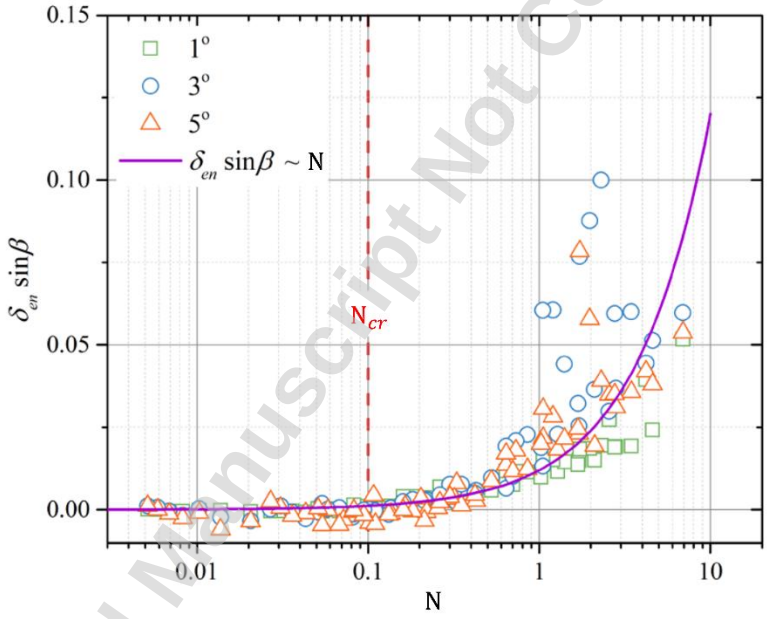

572

573 Fig. 12. The film thickness changed with Stuart number, N, from Yang et al. [89].

574 In addition, as the liquid film boundary layer develops, increased flow resistance
575 leads to liquid accumulation. After surpassing the critical point, the thickness of the
576 liquid film suddenly increases, and the state pressure generated by gravity maintains the
577 process, resulting in a hydraulic jump. The formation of a hydraulic jump is also related
578 to flow separation, separation bubbles, or recirculation vortices at the bottom. After the
579 formation of the hydraulic jump, the liquid level at the hydraulic jump will suddenly

increase and the flow rate will slow down [100]. In the absence of a magnetic field, the position of the hydraulic jump is related to factors such as flow rate, viscosity, and gravity [101]. For a plane hydraulic jump [102], the position of a hydraulic jump can be expressed as $x_j \propto (Q/w)^{5/3}\nu^{-1}g^{-1/3}$, where Q is the flow rate, w is the width of the channel. In the experiments of Fisher et al. [103], the hydraulic jump position moved downstream under the influence of the transverse magnetic field (Fig. 13), which may be because the MHD drag suppressed the turbulent disturbance. In addition, experiments on lithium film flow under transverse field influence have shown that liquid lithium can be trapped at an inlet of an experimental setup, preventing it from flowing downstream [99]. Moreover, the MHD effect reduces the height ratio across the hydraulic jump. As the magnetic field increases, the type of hydraulic jump will also be changed. The hydraulic jump is completely suppressed when the magnetic field intensity reaches a certain value. The height ratio can reflect the energy dissipation of the hydraulic jump [104].

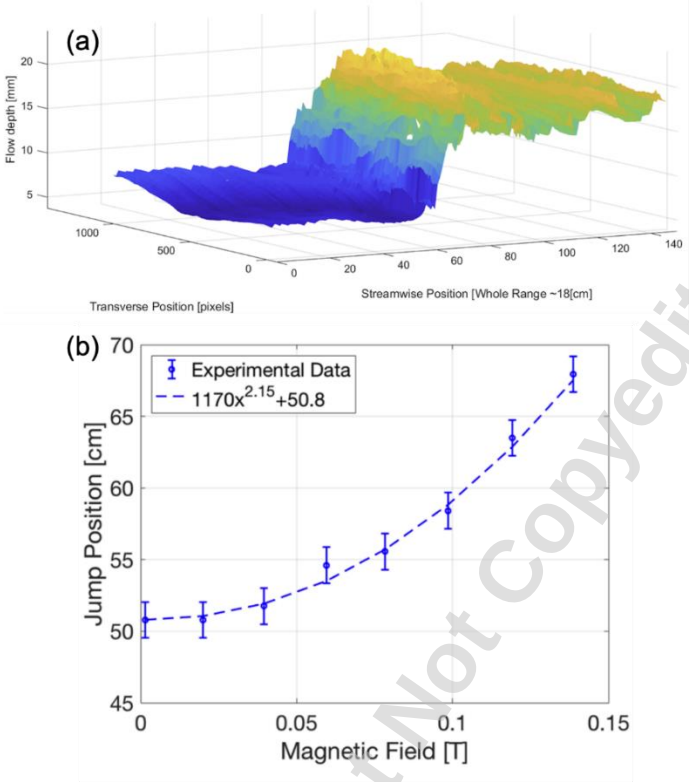

Fig. 13. The hydrodynamic jump [103]. (a) Sample imaging of a hydraulic jump using laser sheet diagnostic, (b) Jump position changes with a magnetic field. Copyright by the AIP Publishing (2018). Reproduced with permission.

3.4 Controlling of free surface flow

For an engineering application such as the liquid metal film flow on PFCs in a nuclear fusion reactor, the stable and uniform thickness of liquid film flow is very important for the design of PFCs. Therefore, many efforts were exerted to reduce the MHD effects by changing the electrical conductivity of the wall and adding external force by introducing a current or thermal gradient.

Concerning the change in wall electrical conductivity, the current will be closed through the Hartmann layers and the side layers for insulating walls, while for

conductive walls, most of the current will pass through the wall. Therefore, the velocity distribution caused by different wall conductivity is also different. According to the distribution of current density of duct flow, the induced current near the side layer is parallel to the magnetic field, while the current near the Hartmann layer is perpendicular to the magnetic field. Therefore, the unique "M-shape" velocity distribution, characterized by two velocity peaks located away from the walls but not at the exact center of the channel and a lower velocity trough in the middle appeared [57]. Similarly, for the liquid metal film flow, the velocity near the side layers is faster than the flow near the Hartmann layers and core flow. Under the influence of the transverse magnetic field, the side layers are distributed near the free surface and the bottom boundary layer, and the thickness is proportional to $\mathrm{Ha}^{-1/2}$. In addition, since the friction force on the free surface is much smaller than the friction force between the liquid and the solid bottom wall, a free surface jet is formed [105,106]. According to Sun's experimental data, the free surface velocity increased by 300%, while the average velocity decreased by 45% [98]. Moreover, they also checked the influence of wall conductivity on the film thickness. Both experimental and numerical simulations have demonstrated that the difference in liquid film thickness between the inlet and outlet grows as the wall conductance ratio increases. Consequently, to minimize MHD drag, selecting materials with a lower wall conductance ratio is preferable.

The introduction of an external current to the liquid metal flow can also have the chance to control the liquid metal free surface flow [74]. Hvasta [107] demonstrated that the thickness and velocity of the liquid metal flow can be controlled by applying

electric and magnetic fields. Meng et al. [108] examined the impact of varying current directions on the free surface flow of liquid metal within a transverse magnetic field environment. For cases with a reverse current, which can generate a vertically downward external Lorentz force, the liquid film becomes thinner in the middle and thicker on both sides. Vise versa, when adding a forward current, which can generate a vertically upward Lorentz force, the liquid column will form on the surface of the liquid film when the amplitude of the current exceeds a certain value. However, due to the increase in the overall thickness of the liquid film, splashing and other phenomena will not occur. In particular, to get closer to the real situation in fusion reactors, Smolentsev [97] investigated the influence of a constant wall-normal magnetic field and an azimuthal magnetic field component that varies along the radius of the symmetric geometry on the flow of a thin film which is on the surface of an axisymmetric structure. The azimuthal component of the Lorentz force generated by the interaction between the wall-normal magnetic field and the current in the flow plane causes secondary flow, which eventually forms a swirl flow, and the direction of flow rotation depends on the current distribution. The induced currents near the free surface and the substrate are in opposite directions, so the fluid rotates in two directions. However, when the applied current intensity is strong enough, the fluid rotates in only one direction, and the rotation effect is not suppressed.

Moreover, the thermoelectric effect (Seebeck effect) is created due to the uneven temperature distribution and can also introduce an external electric current, resulting in a Lorentz force to influence the liquid metal flow [109-111]. As the

temperature gradient increases, the flow rate will also increase, allowing for better heat exchange and reducing the impact of local high heat fluxes [112].

3.5 Free surface flow related to nuclear fusion

Compared with solid PFCs, liquid metal PFCs are more conducive to the operation of fusion reactors at higher heating powers due to their good heat transfer characteristics. Because lithium is low-Z, the core plasma has a higher tolerance for lithium. At the same time, lithium can also reduce other impurity levels and temperature gradients in the plasma [6].

The liquid film with a curved bottom wall can better adapt to the gradient magnetic field, but the flow is also more difficult to control. Therefore, Zhang [65] proposed the concept of a multiplayer MHD liquid film that can flow stably. This system mainly consists of a base layer, an adjustment layer, and a stabilization layer. It achieves stable and well-spread film flow by adjusting the distance between the metal mesh and the bottom wall. Special lithium metal infused trenches (LiMIT) have also been designed for liquid metal divertor, which can remove high heat fluxes by using the thermoelectric magnetohydrodynamics (TEMHD) [110].

In the tokamak environment, the plasma can accidentally impact the surface of liquid metal PFCs, resulting in the corresponding Kelvin-Helmholtz (K-H) [66], Rayleigh-Taylor (R-T) [113] and Rayleigh-Plateau (R-P) [114] instabilities in free surface flow. Such instabilities have the potential to induce several problematic outcomes, including corrosion of the divertor target and contamination of the core plasma.

673 For Lithium-metal infused trenches (LiMIT), splashing caused by plasma also
674 depends on factors such as the wettability and the width of the trenches [115]. The
675 plasma impact not only deforms the melt surface but also gradually increases the stress
676 inside the melt over time, resulting in the movement of the melt and interface changes.
677 At the same time, the Lorentz force generated by the current from the plasma scraping
678 layer or the hot electrons emitted from the high-temperature surface and the magnetic
679 field will also cause the movement of the liquid metal [116]. In addition, under high heat
680 loads, the boiling and evaporation of the melt will also cause disturbances in the
681 interface. Waves with shorter wavelengths will be suppressed by surface tension, but
682 the amplitude of longer wavelength fluctuations will be rapidly amplified. The
683 nonuniform distributed stress in the molten metal may cause this long-wave instability.
684 In addition, the plasma-molten metal interface has the characteristics of high-density
685 difference and high surface tension, which form K-H instability under the action of
686 plasma shear stress and velocity difference, but the classic phenomenon of K-H
687 instability was not observed in the simulation and experimental results [66,117].
688 If one focuses only on the momentum transport process during plasma shock,
689 the impact effect of the plasma can be simplified to the effect of a moving pressure
690 source [118], which varies in time and space. When the applied pressure moves at a
691 velocity close to the downstream wave propagation speed, it propagates at a rate
692 similar to that of the trough it generates. This results in a continuous decrease in the
693 thickness of the liquid metal, which may lead to dangerous dewetting. Concurrently, the
694 non-local interaction of surface waves causes the troughs generated upstream to align

with those produced later in the oscillation cycle as they propagate downstream. However, when the time scale of the pressure motion is significantly larger than the response time scale of the free surface, the system approaches a quasi-steady state. In contrast, if the time scale of the pressure motion is much smaller than that of the free interface response, the resulting deflection of the free surface remains relatively minimal.

The driving methods of liquid metal in Tokamak include electromagnetic drive [119] and capillary drive [120,121]. Among them, EAST Tokamak uses the electromagnetic control principle in Section. 3.4 to form a continuous liquid lithium film flow on the surface of the divertor target plate [6]. However, due to the nonuniform resistance of the pipeline, the liquid lithium cannot be spread evenly, similar to a liquid column flow, as described in Section. 3.2, resulting in a surface coverage rate of only 30%, and the remaining uncovered surface is severely corroded. The upgraded limiter improves the wetting performance of liquid lithium on the target surface by designing a special capillary structure, improving the uniformity of the channel, and changing the surface material [122,123], and the surface coverage rate is increased to more than 80%. The latest generation of lithium PFCs is designed with metal grooves, which increases the surface coverage rate to more than 95%. It's similar to the LiMIT, which not only enhances the thermo-electromagnetic dynamic flow of liquid lithium but also improves safety [124]. Recently, Yang et al. [125] designed a kind of PFC model and realized the nearly full spreading of Lithium film flow on the stainless-steel surface with microgrooves with a coverage ratio of 97.32%, which is the largest one reported. With

the development of liquid metal PFCs, the structure of the PFCs has been continuously improved, so that the liquid metal can cover the PFCs and operate stably, but there are still some problems

In addition, when the plasma interacts with flowing lithium, a distinct bright light can be seen, the temperature of the liquid lithium increases, evaporation, and droplet sputtering occurs, and the lithium can be detected by spectroscopy far away from the limiter. The dynamics of the droplets is the next topic that will be discussed later.

4 LIQUID METAL DROPLETS IMPACTING

Liquid metal droplet impacting and spreading are also typical kinds of interfacial flow in fluid dynamics. These processes can be significantly influenced by factors such as droplet velocity, surface tension, magnetic fields, and solidification. Understanding these processes is crucial for applications in materials science, manufacturing, and energy technologies. In this section, we focus on the topic of liquid metal droplets wetting, spreading, impacting on solid or liquid surfaces, and colliding with each other under the influence of magnetic fields.

3.1 Wetting properties of liquid metal

Wettability can be defined as the capacity of a liquid to maintain contact with a solid surface and is a critical property in various scientific and engineering fields. For example, the liquid metal PFCs in Tokamak need a free surface flow, as discussed in Sec. 3 cover on the solid surface. Therefore, achieving good liquid metal wetting on the solid

surface (ensuring complete coverage) is a crucial initial step. Here, we introduce the wettability of several typical liquid metals commonly adopted in engineering applications or fundamental studies.

From the fundamental aspect, mercury is often selected as a modeling liquid to study MHD problems in experiments in earlier years. Ellison et al. [126] studied the contact angle of mercury on six different materials as a function of temperature. As shown in Table 1, the temperature range is 25°C to 150°C. Results indicated that contact angles were very high on substrates, ranging at equilibrium from about 130 °C to 145 °C at 25 °C. Although there were significant differences between the dynamic advancing and receding angles, equilibrium was rapidly achieved in all systems, and the residual hysteresis was negligible. Additionally, the temperature coefficient of the contact angle was consistently small and positive across all systems.

Table 1. Contact angle of mercury on polished solid substrates at various temperatures [126]. Here, $\theta_{a,max}$ and $\theta_{a,eq}$ stand for the maximum and equilibrium advanced contact angle, while $\theta_{r,min}$ and $\theta_{r,eq}$ stand for the minimum and equilibrium receded contact angle.

Substrates	Temperature, °C					
	20	50	75	100	125	150
Tungsten						
$\theta_{a,max}$	142	150	155	155	159	160
$\theta_{a,eq}$	130	130	140	137	140	137

$\theta_{r,eq}$	132	132	137	135	141	137
$\theta_{r,min}$	121	110	120	119	123	124
Stainless steel						
$\theta_{a,max}$	146	150	151	158	162	157
$\theta_{a,eq}$	133	134	136	146	142	141
$\theta_{r,eq}$	132	134	138	143	144	141
$\theta_{r,min}$	124	121	120	130	132	130
Nickel						
$\theta_{a,max}$	148	150	156	161	160	165
$\theta_{a,eq}$	139	135	138	146	145	145
$\theta_{r,eq}$	138	134	137	146	146	145
$\theta_{r,min}$	123	116	124	129	133	130
Quartz						
$\theta_{a,max}$	147	144	150	152	155	159
$\theta_{a,eq}$	132	132	124	130	132	136
$\theta_{r,eq}$	134	132	122	131	132	136
$\theta_{r,min}$	115	122	110	122	118	114
Glass						
$\theta_{a,max}$	147	147	152	156	154	159
$\theta_{a,eq}$	133	132	132	136	139	140
$\theta_{r,eq}$	134	130	131	137	137	140

$\theta_{r,min}$	122	112	120	125	126	125
Teflon						
$\theta_{a,max}$	157	162	166	169	175	178
$\theta_{a,eq}$	134	135	137	142	146	147
$\theta_{r,eq}$	132	132	134	145	145	146
$\theta_{r,min}$	104	98	109	119	119	116

Recently, gallium-based alloys (GBAs) have replaced mercury in the fundamental studies of MHD effects due to their excellent properties, such as low toxicity and liquid state at room temperature. Nevertheless, the complex wetting properties of GBAs present a significant barrier to their practical development and utilization. Unlike the wetting behavior of Hg, it is generally found that when exposed to oxygen concentrations above 1ppm, GBAs will quickly form a solid oxide layer of several nanometers on the surface [127, 128]. This oxide layer will provide a certain rigidity to the liquid metal surface, making the GBAs maintain their shape over a large surface area [129-133]. Nonetheless, some experimental results showed that the presence of the oxide film makes GBAs easy to adhere to the surface of almost all materials, such as metals, glass, and various polymers [134-140]. Lin et al. [141] measured the contact angle of E-GaIn on the Cu and graphite surface. For EGaIn/Graphite, the contact angle was about 150°, for EGaIn/Cu, the contact angle decreased to approximately 85°. Dobosz et al. [142] have obtained the contact angle between the Ga-Sn-Zn eutectic and

779 the substrates, with contact angles 132 ± 1° for glass, 118 ± 2° for quartz, and 134 ± 1°
780 for silicon, as shown in Fig. 14. The results indicated that the wetting behavior of Ga-Sn-
781 Zn eutectic alloy is similar in the cases of glass and silicon. The obtained values in the
782 case of silicon are similar to the value obtained in reference [143] for Galinstan on
783 silicon (139° at 303 K).
784

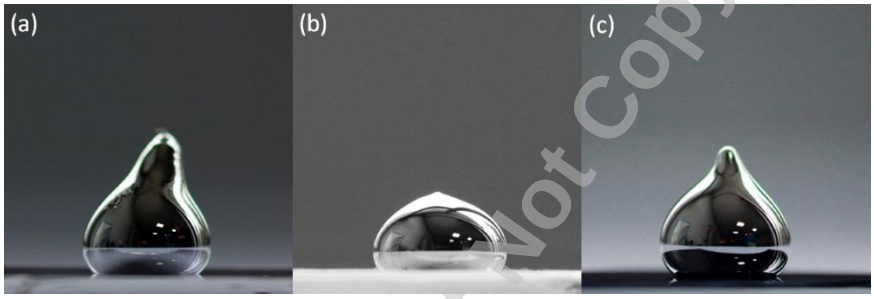

785
786 Fig. 14. Contact angles of Ga-Sn-Zn on three material surfaces: (a) glass, (b)
787 quartz, and (c) silicon [142]. (CC BY 4.0)
788
789 Table 2. Wetting angles of PbBi on the RAFM steel surface based on the ellipse fitting
790 [150].

Temperature (°C)	Wetting angles (°)	
	Left side	Right side
350	148.9073	146.2145
400	150.7129	148.2486
450	145.9786	142.2444
500	144.9476	141.1075

791

According to existing research, two categories are roughly classified to adjust the wettability of GBAs: (i) Formation and removal of the gallium-based surface oxide film and (ii) surface treatment of the LM droplets of the substrates. Considering gallium-based oxide as a pivotal role in liquid metal wetting behavior, researchers tried to facilitate or suppress the oxide formation to enhance or restrain liquid metal wetting and adhesio [133-145]. Guo et al. [146, 147, 148] dispersed Ni, Cu, or Fe nanoparticles evenly into the gallium-based liquid metal, improving its conductivity meanwhile increasing the amount of gallium-based oxide wrapped around the nanoparticles. They found that the obtained semi-solid material had much larger adhesion to many materials and could be easily transferred to paper, PU(Polyurethane), and other substrates. In contrast, Bilodeau et al. [135] eliminated the surface oxide film to reduce liquid metal wetting by a certain concentration of acid or base solution, and Handschuh-Wang et al. [133] found the base more powerful than acid in gallium-based oxide removal. Khan et al. [144] adopted an electrochemical method to deposit or remove the oxide layer on a drop of GBAs in NaOH solution, dramatically changing its wetting behavior.

From aspects of engineering applications, liquid metals with high melting temperatures, such as Lithium lead (PbLi), lithium (Li), and sodium (Na), are commonly adopted. The wetting properties between the liquid metal and the structural materials are important. Ueki et al. [149] measured the contact angle of a molten PbLi droplet on a silicon carbide (SiC) wall at different temperatures (from 250^{o}C to 400^{o}C). Results indicated that the contact angles of all cases are greater than 150^{o}, which could be

814 classified as super-hydrophobic (Fig. 15). Nevertheless, if corrosion of the wall by PbLi
815 occurs, it can be reasonably anticipated that the contact angle will change. Liquid lead-
816 bismuth (PbBi) is a kind of coolant in the Lead-cooled Fast Reactor (LFR). Pan et al. [150]
817 measured the wetting angle of PbBi at reduced activation ferritic/martensitic steel
818 (RAFM steel) surface using the sessile drop method, which was carried out under the
819 protection of high-purity argon. As listed in table 2, experimental results show that the
820 wetting angles of liquid PbBi on RAFM steel are greater than 140° at 350−600°C.
821 Therefore the PbBi also showed the characteristic of superhydrophobic.

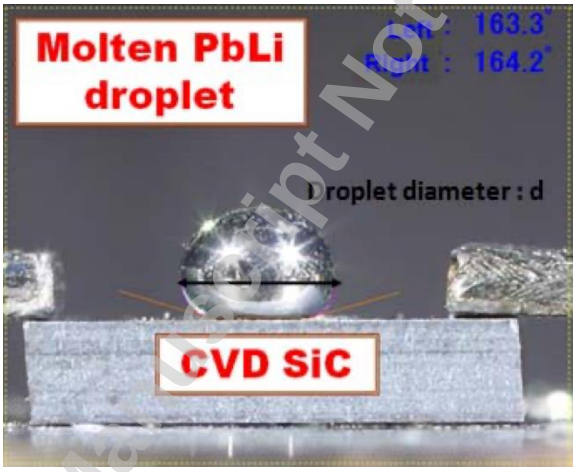

822

823 Fig. 15. A molten PbLi droplet on a CvD SiC (the droplet diameter: 3.2 mm)
824 [149]. Copyright by the Elsevier (2011). Reproduced with permission.

825 Liquid Na is commonly used as a coolant in fast breeder reactors (FBRs) because
826 of its high thermal conductivity, specific heat, low viscosity, low melting temperature,
827 high boiling temperature, and good compatibility with structural materials. In FBR
828 plants, the wettability of structure material owing to the liquid Na content is an
829 important property for safe operation and high efficiency. Saito et al. [151] have
830 investigated the relationship between the contact angle of Na on Cu and its alloys. The

results show that the contact angle of pure Cu is smaller than that of the Cu alloys. The range of the contact angle of all the substrate metals is 110−120°, which is within the standard deviations. Therefore, only slight deviations were noted for the contact angle between the Cu alloys.

4.2 Impingement of droplets on a solid surface

When a liquid droplet impacts the solid surface, various phenomena such as spreading, bouncing, splashing, or sticking can occur due to different impact velocities, surface characteristics, and the physical properties of the liquid. This section focuses on the spreading phenomenon of a class of high-surface-tension liquid metal droplets with/without a magnetic field.

In the absence of MFs, the spreading of metal droplets behaves similarly to that of conventional fluids. This similarity arises because the ratios of physical properties ρ/σ, represented in the dimensionless Weber number, We, $\mathrm{We} = \rho U^2 D/\sigma$, are essentially comparable between liquid metals and conventional fluids like water, here ρ and σ are the density and surface tension of the liquid, U is the impact velocity, D is the diameter of a droplet. However, the spreading behavior of liquid metals is more susceptible to their specific melting points and oxidizing properties. Ahmed et al. [152] investigated the effect of substrate morphology on metal droplet impact behavior. The roughness of the substrate was changed to form different uneven substrates, as shown in Fig. 16. Results revealed that droplet impingement on uneven substrates consistently leads to splashing. However, the intensity of splashing decreased as surface roughness

853 increased since the rougher textures captured and retained more fluid in their gaps,
854 where it then solidified. In contrast, impacts on smoother substrates, which have less
855 roughness, were marked by enhanced splashing due to the liquid being more prone to
856 jetting outward, propelled by its momentum.

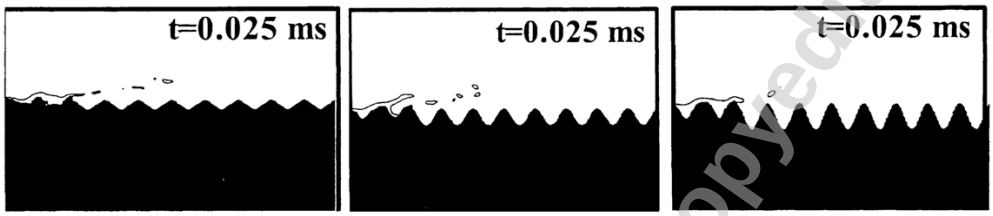

(a) λ =0.4 ε=0.11 (b) λ =0.4 ε=0.22 (c) λ =0.4 ε=0.33

857

858 Fig. 16. Liquid metal droplet spreading on substrates with different roughness
859 [152]. Copyright by the Elsevier (2002). Reproduced with permission.

860 Solonenko et al. [153, 154] performed a comparative analysis of how hollow and
861 solid zirconium oxide droplets deposit on surfaces. The study showed that hollow
862 droplets tend to form smoother films than solid droplets. Kumar and Gu [155] employed
863 the VOF method to examine the impact of hollow tin droplets on a wall, revealing a
864 significant correlation between the gas phase distribution and the dynamic morphology
865 of the droplets upon impact. Dhiman and Chandra [156] observed that at elevated wall
866 temperatures, the edge of the tin droplet solidifies at a slower rate, allowing for more
867 extensive spreading with minimal resistance. Conversely, at lower wall temperatures,
868 the solidification rate of the droplet edge increases significantly, substantially inhibiting
869 its spread. Ogura et al. [157] investigated the spreading behavior and deposition
870 thickness of molten copper using a 0.5 kg sample. Their findings suggest that the melt
871 mass is a crucial factor influencing the spreading area. Several recent studies [158, 159,

160] on 3D printing used metal droplets with high surface tensions, but their impact speeds were very low. To simulate a more realistic engine environment, Li et al. [161, 162] developed an experimental system to study the impact of high-temperature aluminum droplets on solid surfaces. By comparing the dynamic behavior of droplets on surfaces with varying inclinations, they investigated the rebound characteristics of the aluminum droplets. Based on comprehensive experimental data and the principle of energy conservation, they developed a model to calculate the rebound coefficient of aluminum droplets and found a method to quantitatively determine the residual energy of the droplets during the collision process. Furthermore, Li et al. [163] investigated the heat transfer processes during the collision of high-temperature aluminum droplets on an inclined wall. Their findings indicated that the temperature at the impact point undergoes a two-stage reduction: an initial rapid decrease followed by a slower decrease as the droplet spreads along the wall.

For gallium-based metal droplets, which are liquid at room temperature, much research has focused on their spreading properties on different material surfaces, such as Au, PU, diamond, and graphene [164-166]. Moreover, by changing the surface roughness, it has been demonstrated that the rebound properties of gallium-based metal droplets after impacting were enhanced [128, 140]. Meanwhile, results also proved that the applied SiO_2 microparticles to solid surfaces could adjust the adhesion of gallium-based metal droplets on solid surfaces [138]. Zhang et al. [167] created nano-scale surface roughness on PDMS, copper, and stainless steel using femtosecond laser (fs-laser) ablation, achieving surfaces with significant hydrophobicity against liquid

metal. Nano-second laser (ns-laser) is also effective in creating fine surface microstructures, imparting properties such as super-hydrophobicity [168, 169], superhydrophobicity [170], and ultra-anti-reflection [171], and is more accessible and cost-effective. Therefore, ns-laser was selected to prepare structured metal surfaces for this study. The wetting behaviors of eutectic gallium-indium alloys (GaInSn, with a melting point of 15.5^{o}C) on ns-laser ablated structured metal surfaces were investigated. Appropriate ns-laser processing methods for H13 steel, copper, 304 stainless steel (SS), and tantalum were explored. Surfaces with a wide range of surface roughness, compositions, and various micro-patterns were prepared, and the relationships between these factors and the wetting behavior of liquid metal were thoroughly examined.

When considering the effect of the magnetic field on the spreading characteristics of metallic droplets, the outcomes become highly complex due to the anisotropic nature of the magnetic field, which varies depending on the angle between the magnetic field and gravity. Tagawa [172] carried out numerical simulations on an initially cubic droplet falling onto a flat wall in a uniform static magnetic field. Their findings revealed that when a horizontal magnetic field was applied, droplet spreading tended to become two-dimensional (2D), while a vertical magnetic field application resulted in the electromagnetic force dampening the spread. However, his analysis remains limited to a qualitative description due to the lack of a clear explanation of droplet deformation. Yang et al. [173] obtained the experimental data of a GaInSn droplet spreading on a glass surface in a horizontal magnetic field using a high-speed

imaging method. The impact velocity ranges from 0.1 m/s to 1.2 m/s and the magnetic field can adjust from 0 T to 1.6 T. As shown in Fig. 17, an elliptical spreading pattern of the droplet is first observed by experiments. To explain this phenomenon in more detail from a mechanistic perspective and verify the existence of this phenomenon in a wider parameter range. The scaling law for the maximum spreading factor β_m and aspect ratio of the maximum spreading factor κ_m with the relationship of $\beta_m \sim \mathrm{WeN}$ and $\kappa_m \sim (\mathrm{WeN})^{1/2}$ were obtained. Zhou et al. [174] conducted an experimental investigation into the spreading characteristics of a GaInSn droplet on a solid substrate under a strong vertical magnetic field, with intensities ranging from 0 to 2.5 T. Initially, several droplet parameters, such as shape, spreading factor, dynamic contact angle, spreading velocity, and rebound behavior post-impact, were analyzed without a magnetic field. The fitting relationship between the maximum spreading factor (β_m) and the Weber number was obtained and compared with existing scaling laws. Additionally, the effect of the vertical magnetic field on these parameters was systematically examined. Quantitative results on β_m and maximum spreading time (t_{Dmax}), varied with the Ha and We number, provide a comprehensive understanding of the spreading dynamics. The relationship between β_m and We under different magnetic field intensities demonstrates that a vertical magnetic field significantly inhibits the spreading of liquid metal droplets.

	C1	C2	C3	C4	C5	C6
R1	Time (ms)	Ha=0 OV	Ha=135.5 OV	Ha=0 FV/SV	Ha=135.5 FV	Ha=135.5 SV
R2						
R3	0					
R4	1	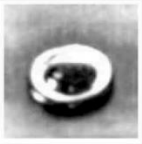	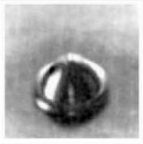			
R5	2	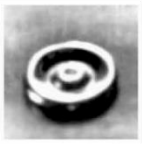				
R6	3	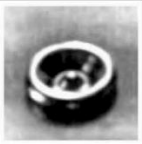	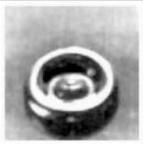			
R7	4					
R8	5					
R9	6					
R10	7					
R11	8					

935

Fig. 17. Snapshots of the spreading process for cases with and without a magnetic field [173]. Copyright by the AIP Publishing (2018). Reproduced with permission.

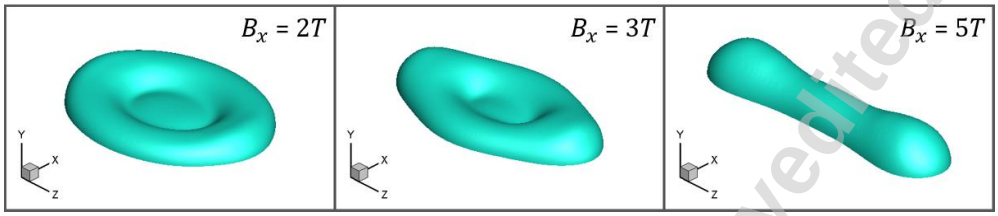

Fig. 18. Droplet Shapes at the moment of the maximum spreading in the *z* direction for the three typical cases [175]. Copyright by the Taylor & Francis (2018). Reproduced with permission.

Han et al. [175] used direct numerical simulation (DNS) to investigate the spreading process of a liquid metal droplet on a flat solid surface in the presence of a horizontal magnetic field. Their simulation results validated the experimental observations by Yang et al. [173], i.e., the elliptical spreading pattern, with the droplet elongated perpendicular to the magnetic field. By extending the experimental parameter, Han et al. [175] found that the droplet looks more like a slender stick than an ellipse when it reaches the maximum spreading, as shown in Fig. 18. Furthermore, given the apparent high surface tension of liquid metals, existing models are not suitable for predicting spreading coefficients. Meng et al. [176] experimentally studied the spreading and rebound characteristics of liquid gallium (Ga) droplets when impacting isothermal and supercooled surfaces under the action of a horizontal magnetic field. Experimental results showed that the magnetic field inhibits the generation of secondary droplets during the spreading and rebound of the droplets

parallel to the magnetic field direction and has a stretching effect on the droplets in the direction parallel to the magnetic field during the rebound process. When the droplet impacts the supercooled wall within a certain range of We values, secondary droplet separation will also occur, and the speed of the secondary droplets generated at this time is relatively small. The intensification of the magnetic field and the increase in the We number contribute to the reduction of droplet oscillation in the vertical direction, thereby accelerating the solidification process.

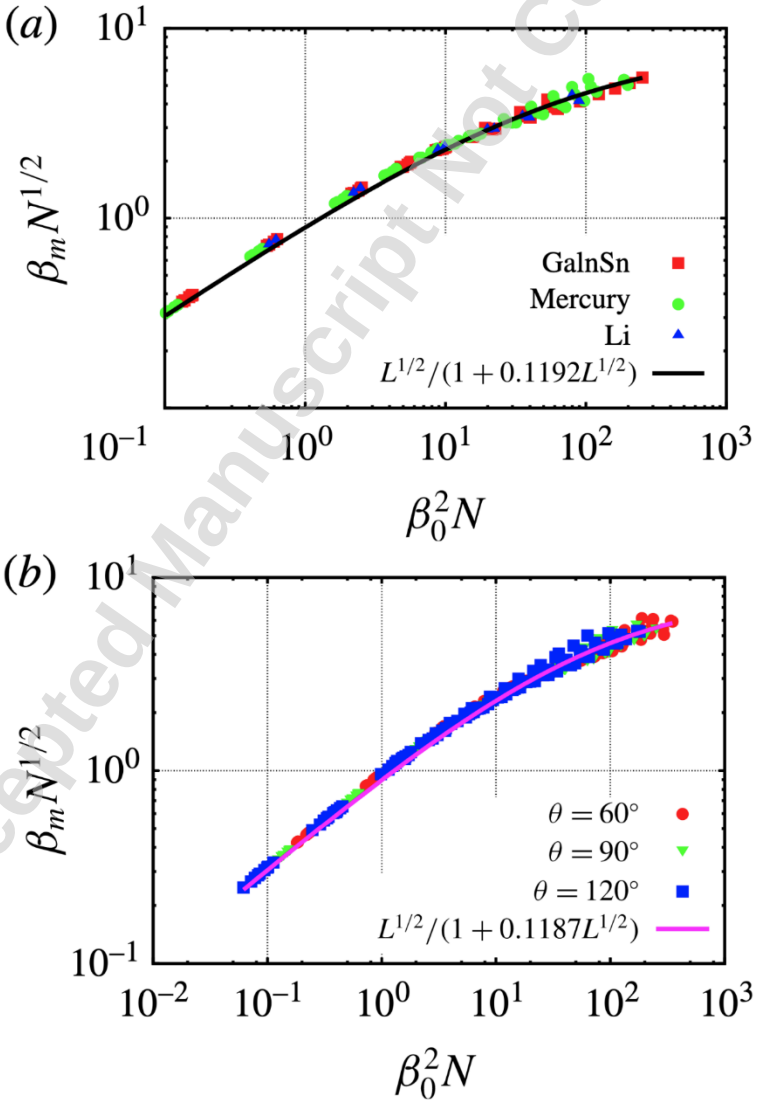

964 Fig. 19. The rescaled maximum spreading ratio as a function of $\beta_0^2 N$, with the
965 solid line showing the interpolating function $\beta_m N^{1/2} = L^{1/2}/\left(1 + BL^{1/2}\right)$ fitted to the
966 numerical results. (a) Numerical results obtained within fixed θ of 90° when using
967 different liquid metals; (b) Numerical results obtained within different θ of 60°, 90° and
968 120° [40]. Copyright by the Cambridge University Press (2016). Reproduced with
969 permission.

970 More recently, we should stress that there are several works to provide
971 quantitative results about the maximum spreading of the impacting droplets under the
972 influence of external magnetic fields. Concerning the influence of vertical magnetic field
973 on liquid metal droplet impacting, Zhang et al. [40] developed a theoretical model to
974 predict the maximum spreading factor by using the principle of energy conversion. The
975 results show that when there is no magnetic field, the maximum factor can be well
976 predicted by an interpolation scheme between the viscous and capillary effects. When
977 gradually increasing the magnetic field strength, the induced Lorentz force dominates
978 over the viscous and capillary forces, causing the spreading behavior to enter the Joule
979 regime. By interpolating it with the viscous dissipation and the capillary effects, a
980 universal scaling law of $\beta_m \propto N^{-1/2} f_c \beta_0^2 N$ is proposed to predict the maximum
981 spreading diameter. All the numerical results are found to rescale onto a single curve
982 predicted by $\beta_m N^{1/2} = L^{1/2}/\left(1 + BL^{1/2}\right)$, as shown in Fig. 19, proving that the
983 theoretical model is correct in predicting the maximum spreading factor by constructing
984 a balanced formula between kinetic energy, capillary energy, viscous dissipation energy
985 and Joule dissipation energy. After that, under the influence of a horizontal magnetic

field, Han et al. [177] developed a new model that considered the anisotropic spreading behaviors produced by the horizontal magnetic fields. In the context of that model, they evaluate the residual kinetic energy due to high surface tension exhibited by the liquid metal and give a more precise estimation of the spreading time than previous works designed for ordinary fluids. Then they incorporate the work of Lorentz force into the energy balance equation, and the theoretical predictions exhibit a very good agreement with the numerical results. Based on these theoretical arguments, Sun et al. [178] conducted numerical simulations to study the solidification behavior of a liquid metal droplet impacting a cold substrate under the influence of a vertical magnetic field, and an interpolation scheme that integrates impact, thermal, and MHD effects is proposed to predict the maximum spreading factor, showing strong agreement with the numerical results. For non-isothermal conditions, solidification transitions the droplet from full rebound to adhesion on the cold substrate, while the magnetic field induces a pinch-off phenomenon during droplet retraction. The mechanisms underlying the transition between different impact regimes are analyzed and compared with existing experimental data and analytical models. Lastly, it is demonstrated that the thickness growth of the solidified sheet can be predicted by solving a simple one dimensional Stefan problem, highlighting the dominance of thermal dynamics over hydrodynamic or MHD effects during the melting of the spreading droplet.

4.3 Impingement of droplets on liquid surface

When a liquid metal droplet impacts a liquid surface instead of a solid one, the outcomes are significantly different due to the change in boundary condition. Li et al. [179] investigated the interaction between a high temperature zirconium dioxide sphere and cold water, discovering that the velocity of the sphere increases with its temperature. Similarly, Zhan et al. [180] investigated the dynamics of high-temperature steel spheres descending into cold water, also concluding that the velocity of these hot spheres rises with their temperature. Li et al. [181] experimentally investigated the moving characteristics of molten metal droplets impact coolant (Fig. 20). Lead-bismuth was chosen as the metal because of its low melting point and water as a cooling coolant. Results showed that the falling velocity of the droplet increases with the droplet's initial temperature when the coolant temperature is invariable. The falling velocity of the droplet increases with the coolant temperature when the droplet's initial temperature is invariable.

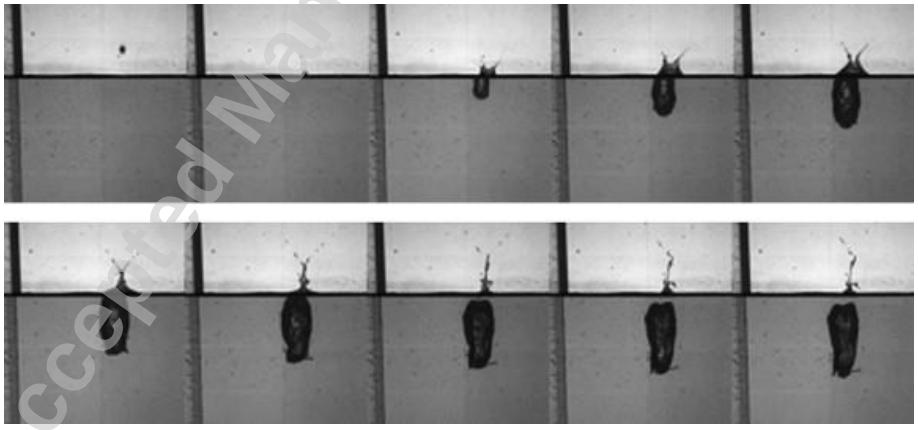

Fig. 20. Experimental images of the experiment condition H790Tw22-Tp334-2000. H: falling distance of molten droplet before it touches the coolant surface, mm; Tw: water temperature, C; Tp: molten droplet temperature, C; 2000: photo-frequency of

the high-speed camera, fps (the time interval between two adjacent photos in the figure is 3 ms) [181]. Copyright by the Elsevier (2008). Reproduced with permission.

The impact of a three-dimensional liquid metal drop onto a film of the same liquid is numerically investigated by Wang et al. [182]. The VOF method combined with adaptive mesh refinement is used for interface tracking, while a consistent and conservative scheme is adopted to calculate the induced current density and Lorentz force. It was found that the perpendicular magnetic field confines the sputtering flow, reduces the crown diameter, and tends to suppress the sputtering flow. However, at sufficiently high falling velocities, the Vertical Magnetic Field (VMF) fails to mitigate the instability, resulting in the ejection of secondary droplets from the crown rim.

Hadj-Achour et al. [183] experimentally investigated the behavior of a molten droplet impact perpendicular to the interface of a deep water pool to characterize the different fragmentation regimes and to develop a relationship for the characteristic size of fragments that can be used in nuclear safety modeling codes. The We number is changed from 10 to 118 with a constant water temperature of 75^{o}C. Their findings indicated that in liquid gas systems, the droplet undergoes various fragmentation regimes depending on its Weber number: oscillations, bag oscillations, prolate drop stretching breakup, and finally, bowl-shaped bag breakup. Additionally, a straightforward relationship between the Sauter Mean Diameter (SMD) and the We number is proposed, grounded in energy and mass balance considerations.

Some researchers also focus on liquid metal droplets impacting the pool of the same materials. Li et al. [184] experimentally investigated the fluid dynamics of room

temperature liquid metal droplet (RTLM) impact onto a pool of the same liquid in ambient air. The experiments varied the impact Fr from 20 to 26, and the We from 479 to 763. The variables set for the study included droplet diameter, impact velocity, and pool temperature. The results indicated that droplet size and impact velocity exhibit similar trends in their effects on splash height, with no secondary droplet separation in either case. However, an increase in pool temperature significantly enhances the splash effect, resulting in the formation of shuttle-shaped secondary droplets detaching from the central jet. This difference is likely due to the oxide scale of the RTLM droplets, which significantly influences the droplet appearance and splash morphology. Energy analysis further supported this hypothesis, clarifying that the oxidation effect primarily alters the viscosity of RTLM.

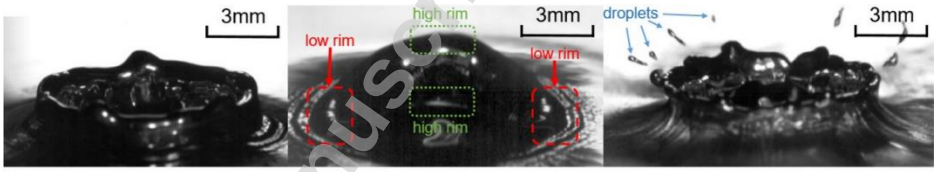

Fig. 21. Typical outcomes of impingement by liquid metal droplets impact the liquid metal film. (a) Symmetric crown, We = 75 and Ha = 0, (b) asymmetric crown, We = 75 and Ha = 174, and (c) prompt splashing, We = 94 and Ha = 0 [185]. Copyright by the Elsevier (2020). Reproduced with permission.

Ren et al. [185] experimentally conducted a study on the impact of high surface tension liquid metal droplets on the same liquid film in the presence of a horizontal magnetic field. They observed three distinct outcomes: symmetric crown, asymmetric crown, and instantaneous splash, with the asymmetric crown being newly identified in

this study (Fig. 21). They systematically examined the influence of variables such as droplet size, impact velocity, initial film thickness, and magnetic field intensity on these results. For crown formation, the external horizontal magnetic field altered the crown shape from symmetric to asymmetric during expansion. In the case of the instantaneous splash, the magnetic field enhanced the splashing effect and reduced the critical Weber number required for instantaneous splashing. This research ultimately demonstrated that the Lorentz force, under the influence of an external horizontal magnetic field, is the primary factor affecting the splashing behavior of liquid metal droplets.

4.4 Collisions between two droplets

Regarding collisions between metal droplets, fewer studies have been carried out due to the difficulty of controlling the droplets and their extreme susceptibility to oxidation, especially including the effects of magnetic field. Menchaca-Rocha et al. [186] conducted experimental investigations on the collision of two mercury droplets in the absence of a magnetic field. The droplets, falling from two 30^{o} ramps, impacted a specially treated horizontal glass surface. They proposed a surface-dynamic nuclear fragmentation model for macroscopic droplet collisions (with diameters up to 5 mm). However, the initial nonspherical shape of the droplets introduced ambiguity regarding whether the observed deformation resulted from the initial shape or the collision itself. Besides, Xia et al. [187, 188] numerically investigated head-on and off center collisions of alumina droplets at 3387 K, conditions under which experimental studies are unfeasible due to the extremely high temperatures.

Jia et al. [189, 190] performed comprehensive experiments on the dynamics of GaInSn droplet collisions without and with the influence of the magnetic field. The experiments covered a broad range of We numbers from 5 to 400 and impact parameters (X, $X = x/D$ where x is the distance between two droplet centers before the moment of impact in the plane perpendicular to the relative velocity vector) from 0 to 1. As shown in Fig. 22, They identified six distinct collision types: coalescence, stretching separation, coalescence after finger formation, separation of finger, break up after finger formation, and stretching separation with finger pinching. Our research revealed that both collision regimes, in the low We number range without finger generation and in the high We range with finger generation, were observable within a relatively narrow range ($\mathrm{We} < 400$) compared to other ordinary liquids.

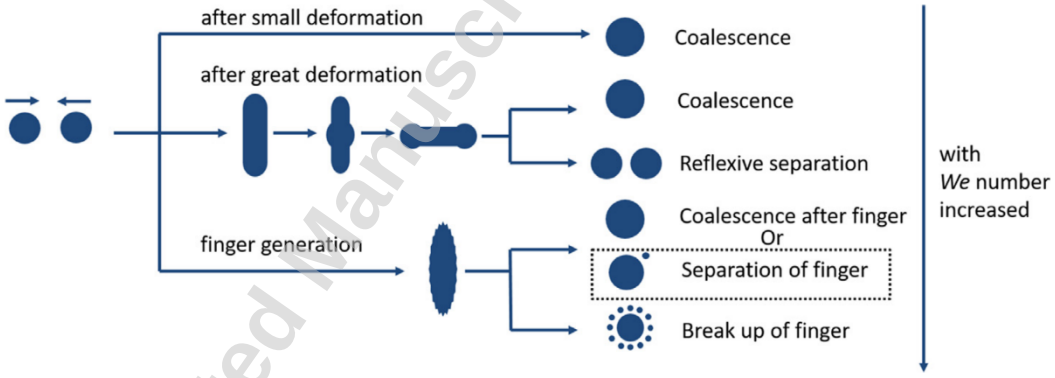

Fig. 22. Schematic of collision regimes for head-on collision with We number increased [189]. Copyright by the Elsevier (2019). Reproduced with permission.

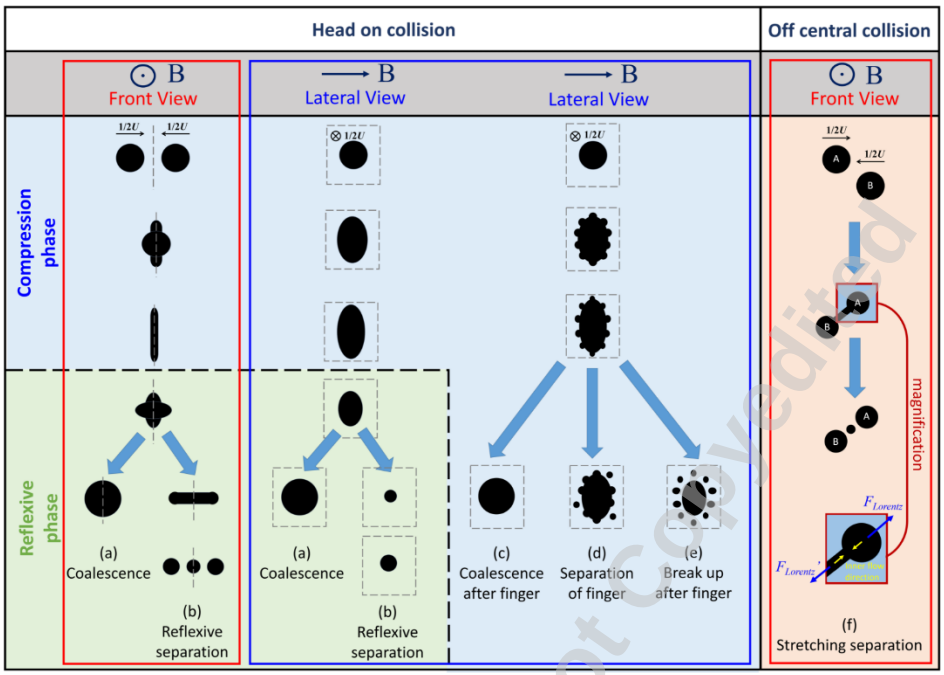

Fig. 23. Possible collisional process for the large intensity of horizontal magnetic field (B > 4T) (the grey dotted squares in lateral view are the cross-sectional drawing of grey dotted lines in front view) [190]. Copyright by the APS (2021). Reproduced with permission.

Additionally, Jia et al. [190] investigated the influence of a horizontal magnetic field on the binary impact dynamics of GaInSn droplets, with magnetic field intensities up to 1.5 T and We numbers ranging from 5 to 200. The results indicate that for a small magnetic interaction parameter ($\mathrm{N} < 0.4$), the collision regime known as reflexive separation is significantly enhanced by the presence of a magnetic field compared to scenarios without a magnetic field (Fig. 23). For collision regimes other than reflexive separation, a correlation that is $\mathrm{N} \sim f(B/B_0, \mathrm{We}/48)$ was proposed. This correlation can help interpret the minimal influence of the magnetic field on these regimes and predict significant effects when the magnetic field strength exceeds a critical value of 4 T.

Furthermore, they delineated the potential geometrical morphology of droplets post-collision, informed by the understanding of the physical processes governing liquid metal droplet collisions under a horizontal magnetic field.

5 BUBBLE MOTION IN LIQUID METAL

To effectively study the influence of magnetic fields on bubbles, it is essential to start with a single bubble, where the key scientific issues include the need to elucidate the mechanisms underlying MF-induced changes in bubble dynamics, particularly in terms of wake modification, velocity modulation, and path transitions. Then, the study of multiple bubbles introduces additional complexities, such as inter-bubble interactions, collective behavior, and their influence on flow structures under magnetic fields. Consequently, this part will draw on insights from both experimental investigations and numerical simulation studies.

The problem of a single bubble rising in liquid metal due to the effect of buoyancy is governed by different non-dimensional parameters, which arise from the governing equations Eqs. (1)~(3). They are the Galilei number, the Bond number, and the magnetic interaction number, expressed as

$$\mathrm{Ga} = \frac{\rho\sqrt{gD}D}{\mu}, \quad \mathrm{Bo} = \frac{\rho g D^2}{\sigma}, \quad \mathrm{Ne} = \frac{\sigma_e B_0^2 D}{\rho\sqrt{gD}}, \tag{19}$$

where D characterizes the bubble's diameter, and other physical properties all belong to the liquid metal. Ga describes the ratio of the buoyant force to the viscous force, Bo is the competition between the buoyant force and the surface tension force, and Ne is the

dimensionless Lorentz force compared to gravity. Besides, the ratio of the physical properties, i.e., the density, the viscosity, and the electric conductivity, between the gas and the liquid metal are also important in determining the rising characteristics of the bubble. However, their values are far smaller than one ($< 10^{-3}$) in the present scenario, and thus the bubble is treated as a massless, slippery, and insulated phase compared to the liquid. In addition, if the terminal velocity u_t of the rising bubble is known as a result, some other non-dimensional parameters can also be defined as

$$\mathrm{Re} = \frac{\rho u_t D}{\mu}, \mathrm{We} = \frac{\rho u_t^2 D}{\sigma}, \mathrm{N} = \frac{\sigma_e B_0^2 D}{\rho u_t}, \mathrm{Ha} = \sqrt{NRe} \tag{20}$$

which are the Reynolds number, the Weber number, the magnetic interaction number, and the Hartmann number respectively, with the characteristic velocity $\sqrt{gD}$ in Eq. 19 replaced by u_t. The remaining important dimensionless parameter to characterize the bubble motion is the Morton number, defined as $\mathrm{Mo} = \mu^4 \rho g / \rho^2 \sigma^3$ which fully relies on the fluid properties. For the liquid metal, note that the density is much greater than that of water (six times for liquid GaInSn and thirteen times for liquid mercury) while their dynamic viscosities are comparable. Essential material properties of liquid GaInSn, which is usually employed in experiments owing to its liquid status at room temperature, and the range of corresponding non-dimensional parameters for a *D* = 5mm sized bubble are shown in Table 3, and for comparison this table also contains the corresponding values for water.

Table 3. Physical properties of the working medium of liquid GaInSn and water, and typical values of dimensionless parameters at a temperature of 20°C for a D = 5mm sized bubble.

	Water	GaInSn
Density, $\rho(kg/m^3)$	998	6361
Dynamics viscosity, $\mu(kg/ms)$	9.8×10^{-4}	2.2×10^{-3}
Electric conductivity, $\sigma_e(\Omega^{-1}m^{-1})$	0.1	3.27×10^{6}
Surface tension, σ (N/m)	0.073	0.553
Morton number, Mo	2.3×10^{-11}	2.4×10^{-13}
Galilei number, Ga	160	340
Bond number, Bo	3.2	2.9
Reynolds number, Re	≈ 1300	≈ 3300
Weber number, We	4.7	2.8

5.1 Rising characteristics of single bubble

Depending on the physical properties of the liquids, the rising trajectory of a single bubble is probably unstable that it may present a zigzag, a spiral, or even a chaos rising behavior [17, 18, 191]. Numerous experimental and numerical studies have been carried out to determine the relationships between the wake structures and the path instabilities of the rising bubble. Particularly, the spiral path was observed to associate

with a continuous wake composed of double-threaded vortex pairs, while the zigzag motion was accompanied by the shedding of hairpin vorticities [18, 192-199]. Moreover, by using different silicon oils, which had a considerable range of viscosity and surface tension, Zenit et al. [200] found that it was actually the aspect ratio of the deformed bubble rather than the Reynolds number that triggered the path instability. Table 3 reveals that the terminal Reynolds number of the rising bubble in liquid metal is significantly higher than that reported in water. As a consequence, the wake structures and the shape evolution of the bubble are significantly more complex in liquid metal than those in water, as identified by Zhang and Ni [39]. However, there are numerous difficulties with experimental measurements of bubble rising in liquid metal. The first challenge is associated with the opacity of these fluid materials, and thus the optical measurement techniques specified for ordinary fluid flow hence cannot be used to get detailed insight into bubble motion. The second problem is the contamination mainly from oxidation, which is known to have a significant impact on the dynamics of rising bubble [201, 202], because the rising bubble no longer persists in fully slippery interfacial condition but behaves more or less like a rigid particle in the presence of contamination [17]. The last difficulty arises because the liquid metals typically have a large surface tension compared to the ordinary fluid, e.g. the surface tension of mercury is $0.487 N/m$ compared to $0.073 N/m$ of water at the room temperature, and thus it is rather difficult to experimentally control the size of the generated bubble [9, 13].

In recent years, different measurement methods have been developed to detect the bubble path and velocity in liquid metals in the presence of external magnetic fields,

essentially to overcome those opacity-induced problems. The measurement techniques can be categorized into intrusive and non-intrusive methods. For the first measurement technique, local conductivity probes [10-12, 203, 204] are used to determine quantities such as the bubble velocity and the bubble size. However, measurements with any local probe disturb the flow in a significant way, especially if the structures to be investigated reach dimensions comparable to the probes. In addition, the Ultrasonic Doppler Velocimetry (UDV) technique, as a typically non-intrusive method, offers a possibility to get information about the flow structure and bubble quantities without flow disruption [9, 205, 206]. UDV overcomes the limitations of traditional probes which can significantly alter the flow field, however, it has to rely on the occurrence of small particles moving with the flow so that the velocity of the bubble can be calculated from the particle position from the time delay between the emitted pulse and the corresponding echo. Consequently, the contamination of those small particles may significantly alter the rising dynamics of the bubble. X-ray radiography [207-209], as another means of non-intrusive approach, has also proven to be an efficient method for bubble detection in liquid metals that is based on the absorption contrast between the liquid and gas phase. However, the main limitation of this technique is the thickness of the fluid volume that can be investigated due to high X-ray absorption coefficients for liquid metals. The other irradiation method relying on neutron radiography is also developed, and it allows for thicker measuring volumes than the X-ray radiograph but at the expense of image contrast [210]. These above-mentioned methods can obtain some information about the rising bubble from a projected two-dimensional (2D) plane but

lack the resolution and adaptability needed for dynamic three-dimensional (3D) analyses. Recent advancements have introduced more powerful techniques, with the Ultrasonic Phased Array (UPA) emerging as a cornerstone in the field [13, 211, 212]. UPA systems use arrays of ultrasonic transducers to generate and detect high-frequency sound waves, enabling detailed tracking of bubble motion in opaque and dynamic environments. They provide real-time 3D visualizations of trajectories, oscillation modes, and distribution patterns of bubbles under various magnetic field conditions. For instance, UPA has been successfully applied to study bubble dynamics in gallium indium tin (GaInSn) alloys, revealing the anisotropic effects of magnetic fields on bubble trajectories and terminal velocities [13, 14]. Another critical advancement is the combination of UPA with other methods such as the Ultrasound Transit Time Technique (UTTT), which provides high-precision measurements of bubble diameters and void distributions in bubble plumes. UTTT resolves the bubble size with an accuracy of less than 7%, making it an indispensable tool for studying bubbles in liquid metals [12, 213]. These techniques have expanded the scope and depth of experimental research, enabling more nuanced explorations of magnetic field effects on bubble behavior.

On the other hand, direct numerical simulation of bubble motion in liquid metals, even for isolated ones, is challenging due to the large differences in density and viscosity between the phases and the high bubble Reynolds number typically encountered, as presented in Table 3. As a result, there are only very few phase-resolving simulations of bubbles in liquid metal under the influence of an MF. Schwarz and Fröhlich [32, 213] proposed an Euler-Lagrange approach for the phase-resolving

simulation of the ascent of a single bubble in liquid metal that an immersed boundary method was implemented to numerically represent the bubble. Such a method enabled them to investigate the bubble motion exposed to a vertical magnetic field (VMF). In the framework of the Eulerian system, Zhang and Ni [19, 39] developed a VOF method to investigate the mechanism of the MHD influence on bubble motion. After that, the method was further developed into a more conservative form by treating the deforming bubble interface as an insulated boundary [25]. Utilizing a similar VOF approach, Jin et al. [20] implemented a ghost fluid method to reduce the spurious flow in the vicinity of the bubble, and the MHD effect of a horizontal magnetic field (HMF) on the bubble motion is investigated.

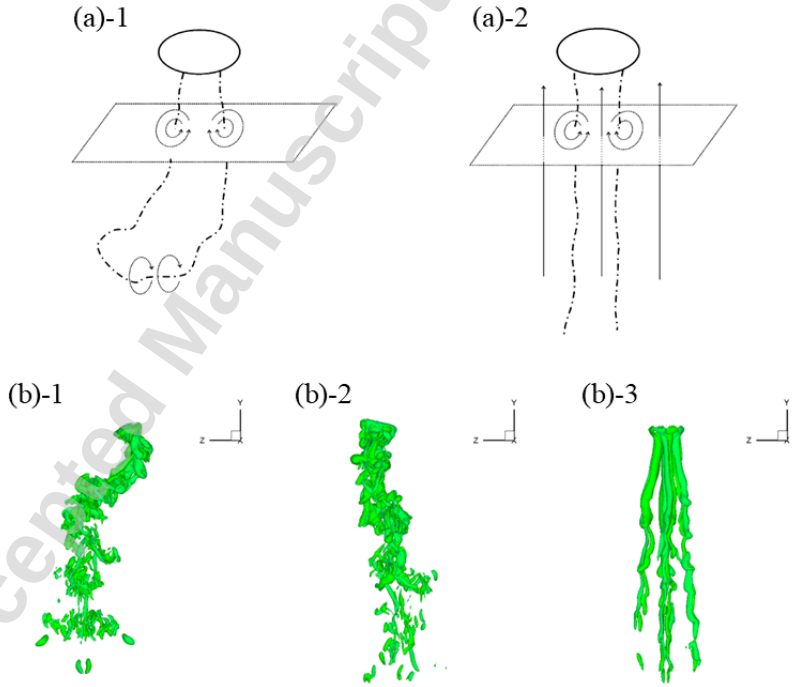

Fig. 24. Variations of vortex structures behind the bubble under vertical magnetic fields. (a) Experimental sketch, the left is without MF while the right is with MF [9], Copyright by the Elsevier (2005). Reproduced with permission.; (b) numerical

results, with N = 0, 0.28 and 0.87 from left to right [39]. Copyright by the AIP Publishing (2014). Reproduced with permission.

Using these advanced measurement techniques and numerical methods designed for bubble motion in liquid metals, experimental studies have yielded valuable insights into how magnetic fields influence the rising characteristics of a single bubble. Under VMFs, Zhang et al. [9] have experimentally reported diverse impacts of VMFs on the terminal velocity of the rising bubble, which depends on the bubble size. For small bubbles ($D \leq 4.6mm$) a decrease of the terminal velocity with increasing magnetic interaction parameter *N* was observed, whereas for larger bubbles ($D \geq 5.4mm$) the application of the magnetic fields increased the terminal velocity. They thought it was because the electromagnetic force would dampen the wake vortices, leading to more rectilinear bubble trajectories when the magnetic field was applied. Such VMF-induced influences on wake structure are sketched in Fig. 24(a), where scenarios without and with magnetic fields are portrayed for comparison. Very recently, the experimental findings reported by Gou et al. [211] further supported such influences caused by VMFs using a UPA technique. They observed that the originally zigzagging oscillation of the bubble was suppressed in a weak VMF ($N < 1$), while the path became an oblique straight-line in moderate VMF ($N \approx 1$), and meanwhile, the terminal velocity of the rising bubble firstly increased and then decreased as the field strength was intensified. A more detailed investigation of the mechanisms caused by VMFs was reported by Zhang et al. [39] utilizing numerical simulations. They found the Lorentz force interacts with bubble-induced electric currents, aligning wake vortices parallel to the field, as shown in

Fig. 24(b). This alignment suppresses wake instabilities and dampens oscillatory forces, leading to more rectilinear and stabilized bubble trajectories, aligning with those experimental measurements. VMFs also deform bubbles, compressing them along the vertical axis while elongating them horizontally due to the pressure distribution modified by the Lorentz force. As the magnetic field strength increases, these effects intensify, further suppressing turbulence in the wake and reducing the bubble's terminal velocity. The magnitude of stabilization and deformation is determined by the interaction parameter, a dimensionless quantity representing the ratio of Lorentz force to inertial forces, with higher values corresponding to greater magnetic field influence. Besides, their numerical study also reported a 'secondary path instability' at sufficiently high VMF strengths, owing to the fact that the field causes a disturbance around the rectilinearly rising bubble, driving the bubble to rise obliquely. This unexpected scenario is recently verified by using a linear stability analysis carried out on a moving sphere in the presence of external VMF [214].

On the other hand, experiments corresponding to HMFs demonstrate that bubble motion transitions from zigzag or spiral patterns to more rectilinear paths at moderate field strengths, while weak fields suppress oscillatory behaviors [16, 206, 215]. Additionally, the most impressive scenario induced by HMFs is the anisotropic in fluence on the rising path of the bubble, and particularly, the oscillatory trajectory persists in the vertical plane perpendicular to the field while it is dampened quickly in the vertical plane parallel to the field. Such anisotropic effects were carefully examined in numerical simulations by Zhang et al. [216, 217] and Jin et al. [20], and the results

reveal that bubble motion becomes anisotropic due to the modification on vortices structures, as shown in Fig. 25(a). The figure shows that in the absence of the magnetic field (N = 0), the twisted vortex structures in the wake region of the bubble are evident, corresponding to a spiral motion of the rising bubble. For N = 0.3 the twisting patterns are decreased and the positive (green) and negative (blue) vortices appear to be more parallel to each other at later times (see t = 51 and 70). As the strength of the magnetic field continues to increase (i.e. for N = 0.5), it can be seen that the twisted vortex structures are fully disintegrated and become mostly parallel due to the anisotropic effect of the HMF on the vortex structures [218, 219]. In other words, the HMFs tend to make the flow field more homogeneous along the direction of the HMF while keeping its structure uninfluenced in the transverse orthogonal direction. In-depth analysis reveals that it is because of the directional electromagnetic forces induced by the MHD effects, which can be described by the current density lines around the bubble in Fig. 25(b). Owing to the vertically electromagnetic force in the vertical plane parallel to the field, as depicted in Fig. 25(c), a Lorentz torque can be produced to offset the pressure gradient along the field direction, and thus the vorticity strength as well as the velocity inhomogeneity are reduced correspondingly. Recent experimental studies carried out by Gou et al. [13], with UPA being applied for accurate exploration of bubble path, revealed transitions in bubble motion modes from random oscillation (R-mode) to perpendicular motion (V-mode), parallel motion (P-mode), and finally straight-line motion (S-mode) with increased HMF intensity. The study also highlighted the correlation between motion modes and terminal velocities, demonstrating that the suppression of

oscillations leads to velocity increases at moderate field strengths but declines at higher intensities due to increased drag.

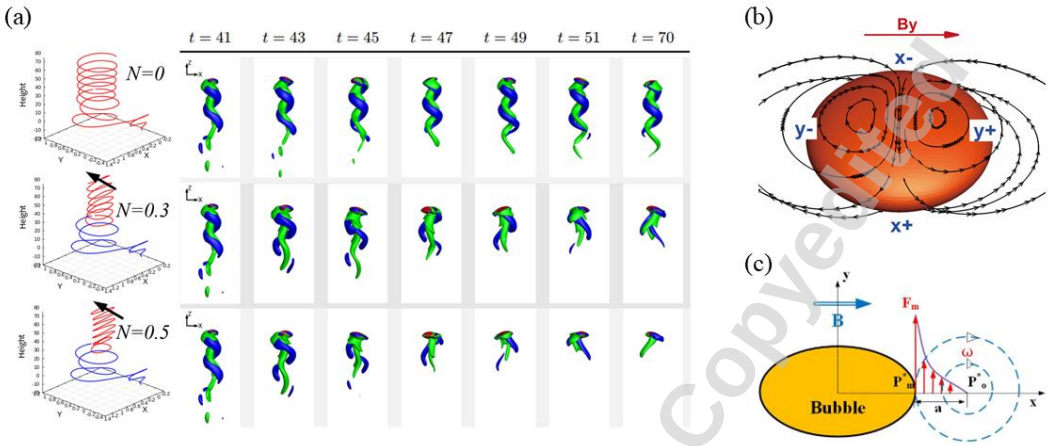

Fig. 25. Anisotropic influences of the HMF on the bubble motion [216, 217]. (a) Suppression of path oscillation in the vertical plane perpendicular to the HMF and the corresponding evolution of the vortices structures; (b) current density lines around the bubble; (c) schematic illustration of the competition between Lorentz force and pressure gradient, generating vortices at both ends of the bubble. Copyright by the AIP Publishing (2016) and Elsevier (2021). Reproduced with permission.

5.2 Rising characteristics of bubble plume

While the dynamics of a single bubble in the presence of external MFs have been extensively investigated, the study of multiple bubbles introduces additional complexities such as inter-bubble interactions, collective behavior, and their influence on turbulent flow structures under magnetic fields [14, 212, 7]. Key scientific questions include understanding the mechanisms of inter-bubble interactions and exploring anisotropic turbulence effects on bubble behavior. Most of the experimental studies

consider the HMFs owing to the restriction of the MF device. Pioneering experimental studies by Eckert et al. [10, 11] were devoted to the lateral dispersion of a bubble swarm in a turbulent liquid metal channel flow in an imposed HMF. The gas phase was injected by a single orifice positioned in the center of the cross-section. An anisotropic distribution of the void fraction arose from a drastic decrease of the bubble dispersion coefficient along the MF lines, whereas moderate damping of the mass transfer properties was observed in the direction perpendicular to the field. The local mass transfer is governed by the anisotropic character of turbulent MHD flows dominated by the existence of quasi-two-dimensional vortices at $\mathrm{Ha} \gg 1$. Such anisotropic findings under the influence of the HMFs are consistent with the scenario reported on a single rising bubble. Later on, Zhang et al. [7] made a quantitative assessment of the bubble plume behavior in the HMF experimentally. They found that in the conventional case without a magnetic field gas bubbles emerge isotropically all over the cross-section, whereas the maximum bubble number was observed at the center. The application of the magnetic field causes a concentration of the bubbles inside a smaller bounded spot. The position of this spot is not fixed but shows a low-frequency oscillation along the diameter of the liquid metal column perpendicular to the direction of the magnetic field. Besides, the original axisymmetric distribution of bubbles became anisotropic with respect to the direction of the MF lines, as shown in Fig. 26. An upwards flow dominated in a plane parallel to the MF, whereas the recirculating motion was enforced in the orthogonal plane. This finding conforms in principle to the results from their previous experimental results [10, 11]. In contrast, VMFs primarily elongate wake structures in

the vertical direction, suppressing small-scale turbulence more effectively than HMFs. This effect creates distinct isotropies in bubble trajectories, as observed in studies where VMFs align bubble paths more strictly along the field lines [11, 212].

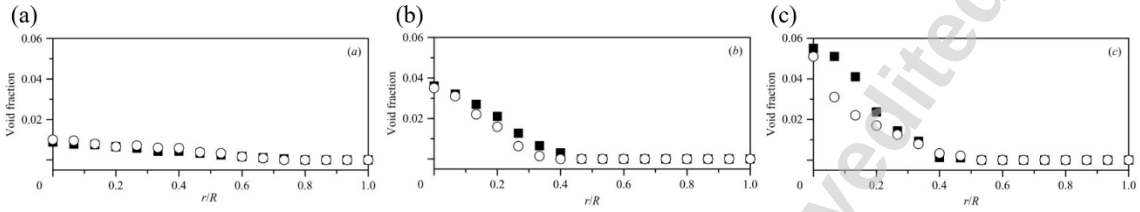

Fig. 26. Time-averaged radial distributions of the local void fraction measured by a conductance probe at various HMFs [7]. (a) Ha = 0; (b) Ha = 271; (c) Ha = 484, closed squares denote the distribution in the vertical plane parallel to the field lines while the open circles are the distribution in the orthogonally vertical plane. Copyright by the Cambridge University Press (2007). Reproduced with permission.

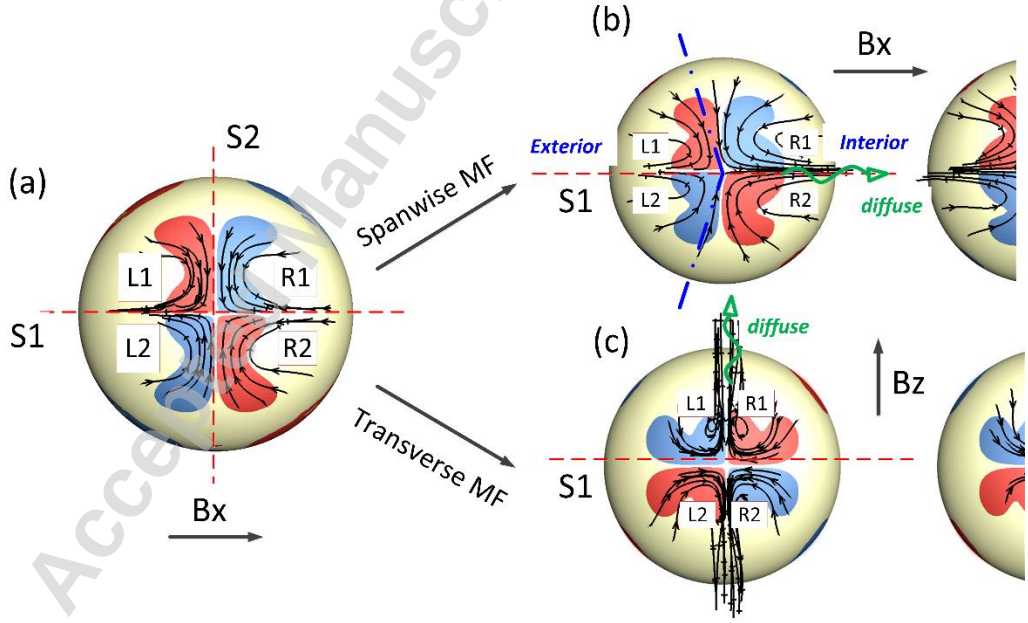

Fig. 27. Sketch showing how the Lorentz diffusion induced vortices evolve in the presence of a neighboring bubble [15]. (a) Single bubble case in a HMF, R1(2) and L1(2)

are the Lorentz diffusion induced streamwise vortices, the black arrow lines are the velocity streamlines, and the green dashed lines denote the double symmetrical planes S1 and S2. (b,c) Bubble pair cases under a spanwise MF and a transverse MF, respectively, and the red arrow lines highlight the diffusion effect along the field lines. Copyright by the Cambridge University Press (2021). Reproduced with permission.

Numerical simulations offer significant advantages over experimental studies in analyzing the motion behavior of multiple bubbles in magnetic fluids because they provide precise control over parameters that are often difficult to manipulate in experimental setups. However, the interplay between the bubble plume and the turbulence flows challenges the accuracy of the numerical simulations, especially in resolving the thin liquid film during bubble-bubble interaction and capturing the very thin boundary layer and the Kolmogorov scale. Miao et al. [220] implemented an Euler-Euler multiphase model into the commercial flow solver CFX, while the turbulent flow was considered by a RANS-CSST turbulence model. Their numerical results reported the destabilization effect of the global flow due to the HMF, which was consistent with the experimental observation mentioned above [7]. Depending on the gas flow rate and the MF strength different transient flow patterns were observed showing strong velocity oscillations with predominant frequencies. This finding appears to be contradictory with respect to the classical studies of the MHD duct flow and is a strong indicator that the relaminarization process of an originally turbulent flow by an applied MF is not fully understood yet for flow configurations deviating from the standard duct flow. Relevant numerical investigations were bubble pair interactions under MFs, as reported by Zhang

and Ni [15], and the results show that bubble interaction and vortex formation were strongly influenced by field strength and orientation. The interaction between a bubble pair is weakened under VMFs, and a transition from bounce to coalescence is observed. In the presence of an HMF, its influences are rather direction dependent and anisotropic: a transverse MF (perpendicular to the bubble-bubble line) always leads the bouncing bubble pair to coalescence, while a spanwise MF (parallel to the bubble-bubble line) has more complex impacts depending on the field strength. Under a spanwise MF, although the flow field is homogenized along the field lines which produce a smaller attractive force by declining the pressure difference at the two sides of the bubble, nevertheless, the Lorentz diffusion also produces double streamwise vortex pairs at the rear of the bubble and the interior pair are stronger in the presence of a neighboring bubble so that a repulsive lift force is induced. As a consequence, the two effects compete with each other on varying the magnetic strength, and thus a weak spanwise MF makes the bubble coalesce while a strong MF causes them to bounce or even to repel. On the other hand, a trans verse MF always promotes the coalescence between the bubble pair because the Lorentz diffusion induces a pair of vortices at an interior position to offset the collision induced vortex pair, and thus the collision between the two bubbles is dampened so that a coalescence is always favored. Such distinctive effects induced by transverse and spanwise HMFs are sketched in Fig. 27. Such bubble pair results also bridge the gap between single bubble motion and bubbly plume in MHD flow, they explain the experimental scenarios why VMFs promote the

coalescence between bubbles and HMFs produce anisotropic distribution between the bubbles.

6 CONCLUSION

6.1 Summary

In the present review, we focus on the interfacial flow of liquid metal with high surface tension related to the PFCs in the Tokamak system and electrometallurgy. Recent progress on the corresponding liquid metal free surface flow, droplet impingement, and bubble motions in liquid metal under the influence of a magnetic field are summarized. According to the MHD theory, the anisotropy of the magnetic field significantly influences the dynamics, transport properties, wave behavior, and energy dissipation rates in liquid metal flow, impacting their stability and efficiency in various applications. When the magnetic field orientation varies in angle relative to the flow direction, its impact on interfacial flow is distinctly different.

MHD effects of free surface liquid metal flow. For the free surface liquid metal flow, the stability of the flow is easily affected by the wettability of solid walls, temperature difference, and various disturbances at the interface. The introduction of electromagnetic forces by the presence of a magnetic field makes the flow more complex. The magnetic field has a generally stabilizing effect on the free surface liquid metal flow by changing the 3D surface waves to Q2D surface waves and ultimately removing all surface waves at a very strong magnetic field. Meanwhile, due to the presence of MHD drag, the thickness of the liquid film increases dramatically with the

increase of Stuart number, N, showing a linear relationship. Results also indicated that by introducing the external current, temperature differences, and changing the electric conductivities of walls, it is possible to find a good solution to drive the flow, reduce the MHD drag, and therefore control the free surface of liquid metal. Till now, many kinds of liquid metal PFCs are under testing.

MHD effects of liquid metal droplet dynamics. When the direction of magnetic field lines aligns with the direction of droplet impact, the magnetic field inhibits the radial spreading of the metal droplet, Characterized by a scaling law relationship for the maximum spreading coefficient, $\beta_{max} \propto \mathrm{N}^{-1/2} f_c(\beta_0^2 \mathrm{N})$. However, when the direction of the magnetic field is perpendicular to the direction of droplet impact, the spreading of the droplet exhibits anisotropy. Specifically, the spreading along the direction of the magnetic field lines is compressed while it is stretched in the perpendicular direction. Further research has also established a relationship between the average maximum spreading coefficient and the strength of the magnetic field.

Bubble dynamics. The MHD influence on the rising dynamics of the bubble motion significantly depends on the MFs strength and orientation. Either the VFM or HMF tends to homogenize the flows along the field lines, hence the vorticity magnitude and the path oscillation inclined to that direction are reduced correspondingly, leading to a larger terminal rising velocity at weak to-moderate MF but a smaller terminal rising velocity at moderate-to-strong MF. Owing to such influence on the vortice structures, the distinctive distribution of volume fraction can also be expected and understood for bubbly plumes under different MFs.

6.2 Open questions

There is still a significant amount of work to be carried out for the free surface liquid metal flow from both engineering and fundamental aspects to promote the realization of liquid metal PFCs. Since the magnetic field lines in the Tokamak system are not in a single direction but comprise multiple components, future research could explore the stability of liquid metal free surface flows under complex magnetic field conditions. When high-temperature plasma interacts with the free surface of liquid metal, the induced surface pressure and significant temperature differences can cause extreme instabilities on the liquid metal surface, leading to phenomena such as liquid metal evaporation and splashing. The stability of free surface liquid metal flows under coupled magnetic and thermal conditions will be a particularly challenging area of research in the future. From the aspect of engineering applications of liquid metal PFCs, more efforts should be put into achieving stable liquid metal film flow by improving the wetting of liquid metal on solid surfaces since most experimental results showed that liquid metals exhibit hydrophobic characteristics on solid surfaces, with corresponding contact angles well over 90°. To overcome the MHD drag, which may stop the liquid metal flow, suitable insulating material should be used to produce the PFC.

The understanding of the MHD effects in realistically complex systems of the bubbly plume is far from complete. Our understanding of the MHD effects on bubbly flows is largely limited to flows with a moderate number of bubbles, while real liquid metal flows in fusion reactors and metallurgic engineering are much more complex that the number of bubbles is nearly $O(10^6)$ or even more. More realistic and efficient

numerical methods should be developed to accurately simulate the bubbly flows under the influence of the MFs, to provide more insights into how the bubbles' motion interacts with the MHD turbulence.

ACKNOWLEDGMENT

We would like to thank Dr. Jiandong Zhou, Dr. Xiaotong Ma and PhD student Linling Li of Xi'an Jiaotong University for their help in collecting materials for the review.

FUNDING

National Science Foundation of China with grants 51927812, 5222260 and 12222208.

National Key Research and Development Program of China with grant 2022YFE03130000.

The Strategic Priority Research Program of Chinese Academy of Sciences with grant XDB0790103.

NOMENCLATURE

ρ	density of the immiscible fluids
μ	dynamic viscosity of the immiscible fluids
ν	kinematic viscosity of the fluid
$\boldsymbol{F_l}$	Lorentz force
$\boldsymbol{F_s}$	surface tension force
$\boldsymbol{J}$	the induced current density
$\boldsymbol{B}$	magnetic field
B_0	external magnetic field (constant), T
B_{0x}	external streamwise magnetic field
μ_m	magnetic permeability
η	magnetic diffusivity of the fluid
σ_e	electrical conductivity
ρ_e	electrical resistivity
σ	surface tension coefficient
$\boldsymbol{u}$	fluid's velocity
U	characteristic fluid velocity
φ	induced electric potential
κ	local curvature of the interface

k_r	real part of the wave number
$\boldsymbol{n}$	normal direction of the interface
δ_s	Dirac distribution function
$\boldsymbol{S}$	remaining source term in Eq. (1)
p	pressure
$\boldsymbol{x}_I^k$	the position of the interface in the *k*-th grid
$\boldsymbol{x}_I$	the position of the interface
$\mathcal{F}$	volume fraction the continuous or disperse phase
K	wave number in the flow direction
N_T	Nusselt film thickness
Re	Reynolds number
M	is the same as Hartmann number
Ha	Hartmann number
N	Stuart number
N^*	is defined as $\mathrm{Ha}^2/\mathrm{Re}^2$
Fr	Froude number
We	Weber number
Ga	Galilei number
Bo	Bond number

Ne	dimensionless Lorentz force compared to gravity
Mo	Morton number
N_{cr}	critical Stuart number
P_m	magnetic Prandtl number
$\mathrm{Re_m}$	magnetic Reynolds number
g	gravity acceleration
α	dimensionless parameter equals to $\sigma_e B^2/\rho\omega$
β	Inclination angle of free surface flow
ω	frequency of the wave
k	wave number
h	the thickness of liquid
h_{av}	average thickness under magnetic field
h_0	average thickness without the magnetic field
γ	the ratio of surface tension coefficient to density of liquid
S_ω^c	power spectral density of capillary wave elevation
S_ω^g	power spectral density of gravity wave elevation
P	energy flux
$\tilde{u}$	velocity perturbation
u_t	terminal velocity during the bubble rising

δ_{en}	relative film thickening
Q	flow rate
w	width of the channel
$\theta_{a,max}$	maximum advanced contact angle
$\theta_{a,eq}$	equilibrium advanced contact angle
$\theta_{r,min}$	minimum receded contact angle
$\theta_{r,eq}$	equilibrium receded contact angle
D	diameter of a droplet
β_m	maximum spreading factor during the droplet spreading
κ_m	aspect ratio of the maximum spreading factor
t_{Dmax}	time at maximum spreading
X	impact parameters of two droplets

1492
1493
1494

REFERENCES

[1] Yarin, A. L., 2006, "Drop impact dynamics: splashing, spreading, receding, bouncing," Annual Review of Fluid Mechanics, 38(1), pp. 159–192.

[2] Josserand, C., and Thoroddsen, S. T., 2016, "Drop impact on a solid surface," Annual Review of Fluid Mechanics, 48(1), pp. 365–391.

[3] Morley, N. B., Smolentsev, S., Barleon, L., Kirillov, I. R., and Takahashi, M., 2000, "Liquid magnetohydrodynamics-recent progress and future directions for fusion," Fusion Engineering and Design, 51, pp. 701–713.

[4] Nygren, R., Rognlien, T., Rensink, M., Smolentsev, S., Youssef, M., Sawan, M., Merrill, B., Eberle, C., Fogarty, P., Nelson, B., et al., 2004, "A fusion reactor design with a liquid first wall and divertor," Fusion Engineering and Design, 72(1-3), pp. 181–221.

[5] Tang, Z., Zuo, G., Li, C., Maingi, R., Meng, X., Xu, W., Sun, Z., Qian, Y., Huang, M., Zhang, D., et al., 2020, "Lithium splashing from flowing liquid lithium limiter and its effect on high confinement plasma performance in east tokamak," Nuclear Materials and Energy, 25, p. 100845.

[6] Hu, J., Zuo, G., Ren, J., Yang, Q., Chen, Z., Xu, H., Zakharov, L., Maingi, R., Gentile, C., Meng, X., et al., 2016, "First results of the use of a continuously flowing lithium limiter in high performance discharges in the east device," Nuclear Fusion, 56(4), p. 046011.

[7] Zhang, C., Eckert, S., and Gerbeth, G., 2007, "The flow structure of a bubble-driven liquid-metal jet in a horizontal magnetic field," Journal of Fluid Mechanics, 575, pp. 57–82.

[8] Bai, H., and Thomas, B. G., 2001, "Bubble formation during horizontal gas injection into downward-flowing liquid," Metallurgical and materials transactions B, 32, pp. 1143–1159.

[9] Zhang, C., Eckert, S., and Gerbeth, G., 2005, "Experimental study of single bubble motion in a liquid metal column exposed to a dc magnetic field," International Journal of Multiphase Flow, 31(7), pp. 824–842.

[10] Eckert, S., Gerbeth, G., and Lielausis, O., 2000, "The behaviour of gas bubbles in a turbulent liquid metal magnetohydrodynamic flow: Part i: Dispersion in quasi-two-dimensional magnetohydrodynamic turbulence," International journal of multiphase flow, 26(1), pp. 45–66.

[11] Eckert, S., Gerbeth, G., and Lielausis, O., 2000, "The behaviour of gas bubbles in a turbulent liquid metal magnetohydrodynamic flow: Part ii: magnetic field influence on the slip ratio," International journal of multiphase flow, 26(1), pp. 67–82.

[12] Richter, T., Eckert, K., Yang, X., and Odenbach, S., 2015, “Measuring the diameter of rising gas bubbles by means of the ultrasound transit time technique,” Nuclear Engineering and Design, 291, pp. 64–70.

[13] Gou, H.-Y., Ni, M.-J., and Yao, Z.-H., 2024, “Experimental study of a single bubble’s motion in a liquid metal under a horizontal magnetic field,” Journal of Fluid Mechanics, 988, p. A21.

[14] Keplinger, O., Shevchenko, N., and Eckert, S., 2019, “Experimental investigations of bubble chains in a liquid metal under the influence of a horizontal magnetic field,” International Journal of Multiphase Flow, 121, p. 103111.

[15] Zhang, J., and Ni, M.-J., 2021, “A numerical study of a bubble pair rising side by side in external magnetic fields,” Journal of Fluid Mechanics, 926, p. A22.

[16] Richter, T., Keplinger, O., Shevchenko, N., Wondrak, T., Eckert, K., Eckert, S., and Odenbach, S., 2018, “Single bubble rise in gainsn in a horizontal magnetic field,” International Journal of Multiphase Flow, 104, pp. 32–41.

[17] Magnaudet, J., and Eames, I., 2000, “The motion of high-reynolds-number bubbles in inhomogeneous flows,” Annual Review of Fluid Mechanics, 32(1), pp. 659–708.

[18] Cano-Lozano, J. C., Martinez-Bazan, C., Magnaudet, J., and Tchoufag, J., 2016, “Paths and wakes of deformable nearly spheroidal rising bubbles close to the transition to path instability,” Physical Review Fluids, 1(5), p. 053604.

[19] Zhang, J., and Ni, M.-J., 2014, “Direct simulation of multi-phase mhd flows on an unstructured cartesian adaptive system,” Journal of Computational Physics, 270, pp. 345–365.

[20] Jin, K., Kumar, P., Vanka, S., and Thomas, B., 2016, “Rise of an argon bubble in liquid steel in the presence of a transverse magnetic field,” Physics of fluids, 28(9).

[21] Sommeria, J., and Moreau, R., 1982, “Why, how, and when, mhd turbulence becomes twodimensional,” Journal of Fluid Mechanics, 118, pp. 507–518.

[22] Kim, J., and Moin, P., 1985, “Application of a fractional-step method to incompressible navier-stokes equations,” Journal of Computational Physics, 59(2), pp. 308–323.

[23] Perot, J. B., 1993, “An analysis of the fractional step method,” Journal of Computational Physics, 108(1), pp. 51–58.

[24] Ni, M.-J., Munipalli, R., Morley, N. B., Huang, P., and Abdou, M. A., 2007, "A current density conservative scheme for incompressible mhd flows at a low magnetic Reynolds number. part i: On a rectangular collocated grid system," Journal of Computational Physics, 227(1), pp. 174–204.

[25] Zhang, J., and Ni, M.-J., 2018, "Direct numerical simulations of incompressible multiphase magnetohydrodynamics with phase change," Journal of Computational Physics, 375, pp. 717–746.

[26] Zhang, J., and Ni, M.-J., 2014, "A consistent and conservative scheme for mhd flows with complex boundaries on an unstructured cartesian adaptive system," Journal of Computational Physics, 256, pp. 520–542.

[27] Krasnov, D., Zikanov, O., and Boeck, T., 2012, "Numerical study of magnetohydrodynamic duct flow at high Reynolds and Hartmann numbers," Journal of Fluid Mechanics, 704, pp. 421–446.

[28] Zikanov, O., Listratov, Y. I., and Sviridov, V. G., 2013, "Natural convection in horizontal pipe flow with a strong transverse magnetic field," Journal of Fluid Mechanics, 720, pp. 486–516.

[29] Grigoriadis, D., Kassinos, S. C., and Votyakov, E., 2009, "Immersed boundary method for the mhd flows of liquid metals," Journal of Computational physics, 228(3), pp. 903–920.

[30] Francois, M. M., Cummins, S. J., Dendy, E. D., Kothe, D. B., Sicilian, J. M., and Williams, M. W.,2006, "A balanced-force algorithm for continuous and sharp interfacial surface tension models within a volume tracking framework," Journal of Computational Physics, 213(1), pp. 141–173.

[31] Tryggvason, G., Bunner, B., Esmaeeli, A., Juric, D., Al-Rawahi, N., Tauber, W., Han, J., Nas, S., and Jan, Y.-J., 2001, "A front-tracking method for the computations of multiphase flow," Journal of Computational Physics, 169(2), pp. 708–759.

[32] Schwarz, S., and Frohlich, J., 2014, "Numerical¨ study of single bubble motion in liquid metal exposed to a longitudinal magnetic field," International Journal of Multiphase Flow, 62, pp. 134– 151.

[33] Osher, S., and Fedkiw, R. P., 2001, "Level set methods: an overview and some recent results," Journal of Computational physics, 169(2), pp. 463–502.

[34] Osher, S., Fedkiw, R., and Piechor, K., 2004, "Level set methods and dynamic implicit surfaces," Applied Mechanics Reviews, 57(3), pp. B15–B15.

[35] Hirt, C. W., and Nichols, B. D., 1981, "Volume of fluid (vof) method for the dynamics of free boundaries," Journal of Computational Physics, 39(1), pp. 201–225.

[36] Gueyffier, D., Li, J., Nadim, A., Scardovelli, R., and Zaleski, S., 1999, "Volume-of-fluid interface tracking with smoothed surface stress methods for three-dimensional flows," Journal of Computational Physics, 152(2), pp. 423–456.

[37] Ni, M.-J., Munipalli, R., Morley, N. B., and Abdou, M. A., 2006, "Validation strategies of himag in interfacial flow computation for fusion applications," Fusion Engineering and Design, 81(8-14), pp. 1535–1541.

[38] Xiao, F., Honma, Y., and Kono, T., 2005, "A simple algebraic interface capturing scheme using hyperbolic tangent function," International Journal for Numerical Methods in Fluids, 48(9), pp. 1023– 1040.

[39] Zhang, J., and Ni, M.-J., 2014, "Direct simulation of single bubble motion under vertical magnetic field: Paths and wakes," Physics of fluids, 26(10).

[40] Zhang, J., Han, T.-Y., Yang, J.-C., and Ni, M.-J., 2016, "On the spreading of impacting drops under the influence of a vertical magnetic field," Journal of Fluid Mechanics, 809, p. R3.

[41] Brackbill, J. U., Kothe, D. B., and Zemach, C., 1992, "A continuum method for modeling surface tension," Journal of Computational Physics, 100(2), pp. 335–354.

[42] Fedkiw, R. P., 2002, "Coupling an eulerian fluid calculation to a lagrangian solid calculation with the ghost fluid method," Journal of Computational Physics, 175(1), pp. 200–224.

[43] Kang, M., Fedkiw, R. P., and Liu, X.-D., 2000, "A boundary condition capturing method for multiphase incompressible flow," Journal of Scientific Computing, 15, pp. 323–360.

[44] Kapitza, P. L., and Kapitza, S. P., 1948, "Wave flow of thin viscous fluid layers," zh. eksp. teor. fiz, 18(1), pp. 3–28.

[45] Benjamin, T. B., 1957, "Wave formation in laminar flow down an inclined plane," Journal of Fluid Mechanics, 2(06), Aug., p. 554.

[46] Kalliadasis, S., Ruyer-Quil, C., Scheid, B., and Velarde, M. G., 2012, Falling Liquid Films, Vol. 176 of Applied Mathematical Sciences Springer London, London.

[47] Hsieh, D.-Y., 1965, "Stability of a conducting fluid flowing down an inclined plane in a magnetic field," Physics of Fluids, 8(10), p. 1785.

[48] Ladikov, Y. P., 1966, "Flow stability of a conducting liquid flowing down an inclined plane in the presence of a magnetic field," Fluid Dynamics, 1(1), Jan., pp. 1–4.

[49] Shen, M., Sun, S., and Meyer, R., 1991, "Surface waves on viscous magnetic fluid flow down an inclined plane," Physics of Fluids A: Fluid Dynamics, 3(3), pp. 439–445.

[50] Rai, L., 1968, "Hydromagnetic stability of a liquid film flowing down an inclined conducting plane," Journal of the Physical Society of Japan, 24(3), pp. 626–632.

[51] Mukhopadhyay, A., Dandapat, B., and Mukhopadhyay, A., 2008, "Stability of conducting liquid flowing down an inclined plane at moderate Reynolds number in the presence of constant electromagnetic field," International Journal of NonLinear Mechanics, 43(7), pp. 632–642.

[52] Giannakis, D., Rosner, R., and Fischer, P., 2009, "Instabilities in free-surface hartmann flow at low magnetic prandtl numbers," Journal of fluid Mechanics, 636, pp. 217–277.

[53] Takashima, M., 1996, "The stability of the modified plane poiseuille flow in the presence of a transverse magnetic field," Fluid Dynamics Research, 17(6), p. 293.

[54] Gotoh, K., 1971, "Hydromagnetic instability of a free shear layer at small magnetic reynolds numbers," Journal of Fluid Mechanics, 49(1), pp. 21– 31.

[55] Murty, G. S., 1961, "Instability of a conducting fluid carrying uniform current in the presence of a homogeneous magnetic field," Arkiv Fysik, 19.

[56] Shercliff, J. A., 1969, "Anisotropic surface waves under a vertical magnetic force," Journal of Fluid Mechanics, 38(2), Sept., pp. 353–364.

[57] Müller, U., and Bühler, L., 2001, "Magnetofluid dynamics in channels and containers," Springer Science & Business Media.

[58] Gao, D., and Morley, N. B., 2002, "Equilibrium and initial linear stability analysis of liquid metal falling film flows in a varying spanwise magnetic field," Magnetohydrodynamics, 38, Dec., pp. 359– 375.

[59] Gao, D., Morley, N., and Dhir, V., 2002, "Numerical study of liquid metal film flows in a varying spanwise magnetic field," Fusion Engineering and Design, 63-64, Dec., pp. 369–374.

[60] Gao, D., and Morley, N., 2004, "Numerical investigation of surface disturbance on liquid metal falling film flows in a magnetic field gradient," Magnetohydrodynamics, 40, Jan.

[61] Dandapat, B., and Mukhopadhyay, A., 2003, "Conducting fluid flowing down an inclined plane in presence of electromagnetic field," International Journal of Applied Mechanics and Engineering, 8(3), pp. 379–383.

[62] Cheng, P.-J., Chen, C.-K., Wang, Y.-C., Lin, M.C., and Yang, C.-K., 2017, "Nonlinear Rupture of Thin Micropolar Liquid Film Under a Magnetic Field," Journal of Mechanics, 33(2), Apr., pp. 249– 256.

[63] Lunz, D., and Howell, P., 2019, "Flow of a thin liquid-metal film in a toroidal magnetic field," Journal of Fluid Mechanics, 867, pp. 835–876.

[64] Lunz, D., 2020, "On thermal axisymmetric liquid metal divertors," Fusion Engineering and Design, 158, Sept., p. 111661.

[65] Zhang, X., Pan, C., and Xu, Z., 2016, "MHD Stability Analysis and Flow Controls of Liquid Metal Free Surface Film Flows as Fusion Reactor PFCs," Plasma Science and Technology, 18(12), Dec., pp. 1204–1214.

[66] Miloshevsky, G., and Hassanein, A., 2010, "Modelling of kelvin–helmholtz instability and splashing of melt layers from plasma-facing components in tokamaks under plasma impact," Nuclear Fusion, 50(11), p. 115005.

[67] Garnier, N., Grigoriev, R. O., and Schatz, M. F., 2003, "Optical manipulation of microscale fluid flow," Physical Review Letters, 91(5), p. 054501.

[68] Lunz, D., 2021, "Minimizing deformation of a thin fluid film driven by fluxes of momentum and heat," Physical Review E, 103(3), Mar., p. 033105.

[69] Goussis, D., and Kelly, R., 1990, "On the thermocapillary instabilities in a liquid layer heated from below," International journal of heat and mass transfer, 33(10), pp. 2237–2245.

[70] Nield, D. A., 1966, "Surface tension and buoyancy effects in the cellular convection of an electrically conducting liquid in a magnetic field," Zeitschrift fur angewandte Mathematik und Physik ZAMP,¨ 17(1), Jan., pp. 131–139.

[71] Wilson, S., 1993, "The effect of a uniform magnetic field on the onset of steady benard-marangoni´ convection in a layer of conducting fluid," Journal of Engineering Mathematics, 27(2), pp. 161–188.

[72] Hashim, I., and Arifin, N. M., 2003, "Oscillatory Marangoni convection in a conducting fluid layer with a deformable free surface in the presence of a vertical magnetic field," Acta Mechanica, 164(34), Sept., pp. 199–215.

[73] Alpher, R. A., Hurwitz, H., Johnson, R. H., and White, D. R., 1960, "Some Studies of FreeSurface Mercury Magnetohydrodynamics," Reviews of Modern Physics, 32(4), Oct., pp. 758–769 Publisher: American Physical Society.

[74] Murav'ev, E., 1988, "Film mhd flows under conditions of a thermonuclear reactor," Magnetohydrodynamics (Engl. Transl.);(United States), 24(1).

[75] Morley, N., and Tillack, M., 1993, "Examination of stability calculations for liquid metal film flows in a coplanar magnetic field," Magnetohydrodynamics, 29(2), pp. 163–169.

[76] Morley, N. B., and Abdou, M. A., 1995, "Modeling of fully-developed, liquid metal, thin film flows for fusion divertor applications," Fusion Engineering and Design, 30(4), pp. 339–356.

[77] Morley, N. B., Gaizer, A. A., Tillack, M. S., and Abdou, M. A., 1995, "Initial liquid metal magnetohydrodynamic thin film flow experiments in the MEGA-loop facility at ucla," Fusion Engineering and Design, 27, pp. 725–730.

[78] Morley, N., Smolentsev, S., Munipalli, R., Ni, M.J., Gao, D., and Abdou, M., 2004, "Progress on the modeling of liquid metal, free surface, mhd flows for fusion liquid walls," Fusion Engineering and Design, 72(1-3), pp. 3–34.

[79] Ying, A., Abdou, M., Morley, N., Sketchley, T., Woolley, R., Burris, J., Kaita, R., Fogarty, P., Huang, H., Lao, X., et al., 2004, "Exploratory studies of flowing liquid metal divertor options for fusion-relevant magnetic fields in the MTOR facility," Fusion Engineering and Design, 72(1-3), pp. 35–62.

[80] Fulford, G. D., 1964, "The Flow of Liquids in Thin Films," In Advances in Chemical Engineering, Vol. 5. Elsevier, pp. 151–236.

[81] Falcon, E., and Mordant, N., 2022, "Experiments in surface gravity capillary wave turbulence," Annual Review of Fluid Mechanics, 54(1), Jan., pp. 1–25.

[82] Vieweg, P. P., Kolesnikov, Y., and Karcher, C., 2022, "Experimental study of a liquid metal film flow in a streamwise magnetic field," Magnetohydrodynamics, 58(12), pp. 5–12.

[83] Liu, J., and Gollub, J. P., 1994, "Solitary wave dynamics of film flows," Physics of Fluids, 6(5), May, pp. 1702–1712.

[84] Michel, G., Semin, B., Cazaubiel, A., Haudin, F., Humbert, T., Lepot, S., Bonnefoy, F., Berhanu, M., and Falcon, E., 2018, "Self-similar gravity wave spectra resulting from the modulation of bound waves," Physical Review Fluids, 3(5), May, p. 054801.

[85] Falcon, E., Fauve, S., and Laroche, C., 2007, "Observation of Intermittency in Wave Turbulence," Physical Review Letters, 98(15), Apr., p. 154501.

[86] Nazarenko, S., 2011, Wave Turbulence, Vol. 825 of Lecture Notes in Physics Springer Berlin Heidelberg, Berlin, Heidelberg.

[87] Zakharov, V. E., 1965, "Weak turbulence in media with a decay spectrum," Journal of Applied Mechanics and Technical Physics, 6(4), July, pp. 22– 24.

[88] Yang, J.-C., Qi, T.-Y., Ni, M.-J., and Wang, Z.H., 2016, "Flow patterns of GaInSn liquid on inclined stainless steel plate under a range of magnetic field," Fusion Engineering and Design, 109111, Nov., pp. 861–865.

[89] Yang, J.-C., Qi, T.-Y., Ren, D.-W., Ni, M.-J., Liu, B.-Q., Hu, J.-S., and Li, J.-G., 2020, "Magnetohydrodynamic effects on liquid metal film flowing along an inclined plate relating to plasma facing components," Nuclear Fusion, 60(8), Aug., p. 086003.

[90] Narula, M., Abdou, M., Ying, A., Morley, N., Ni, M., Miraghaie, R., and Burris, J., 2006, "Exploring liquid metal plasma facing component (PFC) concepts—Liquid metal film flow behavior under fusion relevant magnetic fields," Fusion Engineering and Design, 81(8-14), pp. 1543-1548.

[91] Ying, A., Abdou, M., Morley, N., Sketchley, T., Woolley, R., Burris, J., Kaita, R., Fogarty, P., Huang, H., Lao, X., Narula, M., Smolentsev, S., and Ulrickson, M., 2004, "Exploratory studies of flowing liquid metal divertor options for fusion relevant magnetic fields in the MTOR facility," Fusion Engineering and Design, 72(1-3), Nov., pp. 35–62.

[92] Zhu, L., Feng, Y., Ye, X., and Zhou, Z., 2006, "Tuning wettability and getting superhydrophobic surface by controlling surface roughness with well designed microstructures," Sensors and Actuators A: Physical, 130-131, pp. 595–600.

[93] Rhoads, J. R., 2013, "Magnetohydrodynamics and heat transfer in a free-surface, flowing liquid metal experiment," PhD thesis, Princeton University. https://dataspace.princeton.edu/handle/88435/dsp01rj430467r

[94] Ji, H., Fox, W., Pace, D., and Rappaport, H. L., 2004, "Study of small-amplitude magnetohydrodynamic surface waves on liquid metal," Physics of Plasmas, 12(1), Nov., pp. 012102–012102–13.

[95] Platacis, E., Flerov, A., Klukin, A., Ivanov, S., Sobolevs, A., Shishko, A., Zaharov, L., and Gryaznevich, M., 2014, "Gravitational flow of a thin film of liquid metal in a strong magnetic field," Fusion Engineering and Design, 89(12), Dec., pp. 2937–2945.

[96] Nornberg, M. D., Ji, H., Peterson, J. L., and Rhoads, J. R., 2008, "A liquid metal flume for free surface magnetohydrodynamic experiments," Review of Scientific Instruments, 79(9), Sept., p. 094501.

[97] Smolentsev, S., and Abdou, M., 2005, "Open surface mhd flow over a curved wall in the 3-d thin shear-layer approximation," Applied mathematical modelling, 29(3), pp. 215–234.

[98] Sun, Z., Al Salami, J., Khodak, A., Saenz, F., Wynne, B., Maingi, R., Hanada, K., Hu, C., and Kolemen, E., 2023, "Magnetohydrodynamics in free surface liquid metal flow relevant to plasma facing components," Nuclear Fusion, 63(7), July, p. 076022.

[99] Liu, B.-Q., Yang, J.-C., Qi, T.-Y., Ren, D.-W., Zhang, J., and Ni, M.-J., 2018, "Experimental study on the lithium film flow in the spanwise magnetic field," Fusion Engineering and Design, 136, Nov., pp. 522–526.

[100] Wang, W., Baayoun, A., and Khayat, R. E., 2023, "A coherent composite approach for the continuous circular hydraulic jump and vortex structure," Journal of Fluid Mechanics, 966, July, p. A15.

[101] Bohr, T., Dimon, P., and Putkaradze, V., 1993, "Shallow-water approach to the circular hydraulic jump," Journal of Fluid Mechanics, 254, Sept., pp. 635–648.

[102] Bhattacharjee, J. K., and Ray, A. K., 2011, "Hydraulic jump," Journal of Physics: Conference Series, 319, Sept., p. 012003.

[103] Fisher, A. E., Kolemen, E., and Hvasta, M. G., 2018, "Experimental demonstration of hydraulic jump control in liquid metal channel flow using Lorentz force," Physics of Fluids, 30(6), June, p. 067104.

[104] Richard, G. L., and Gavrilyuk, S. L., 2013, "The classical hydraulic jump in a model of shear shallow-water flows," Journal of Fluid Mechanics, 725, June, pp. 492–521.

[105] Siriano, S., Tassone, A., and Caruso, G., 2021, "Numerical simulation of thin-film mhd flow for nonuniform conductivity walls," Fusion Science and Technology, 77(2), pp. 144–158.

[106] Molokov, S., and Reed, C., 2000, "Review of free surface mhd experiments and modeling,". Jun. https://doi.org/10.2172/757509

[107] Hvasta, M. G., Kolemen, E., Fisher, A., and Ji, H., 2017, "Demonstrating electromagnetic control of free-surface, liquid-metal flows relevant to fusion reactors," Nuclear Fusion, 58(1), p. 016022.

[108] Meng, X., Wang, Z., and Zhang, D., 2022, "Experimental study on liquid metal free surface flow under magnetic and electric field for nuclear fusion," Nuclear Fusion, 62(3), p. 036029.

[109] Shercliff, J. A., 1979, "Thermoelectric magnetohydrodynamics," Journal of Fluid Mechanics, 91(2), Mar., pp. 231–251.

[110] Ruzic, D., Xu, W., Andruczyk, D., and Jaworski, M., 2011, "Lithium–metal infused trenches (limit) for heat removal in fusion devices," Nuclear Fusion, 51(10), p. 102002.

[111] Jaworski, M. A., Gray, T. K., Antonelli, M., Kim, J. J., Lau, C. Y., Lee, M. B., Neumann, M. J., Xu, W., and Ruzic, D. N., 2010, "Thermoelectric Magnetohydrodynamic Stirring of Liquid Metals," Physical Review Letters, 104(9), Mar., p. 094503.

[112] Xu, W., 2015, "Experimental and numerical analysis of thermoelectric magnetohydrodynamic driven liquid lithium flow in open channels for fusion applications," PhD thesis, University of Illinois at Urbana-Champaign. https://www.ideals.illinois.edu/items/79861/bitstreams/209351/data.pdf

[113] Jaworski, M., Abrams, T., Allain, J., Bell, M., Bell, R., Diallo, A., Gray, T., Gerhardt, S., Kaita, R., Kugel, H., et al., 2013, "Liquid lithium divertor characteristics and plasma–material interactions in NSTX high-performance plasmas," Nuclear Fusion, 53(8), p. 083032.

[114] Mesyats, G., and Zubarev, N., 2015, "The rayleigh–plateau instability and jet formation during the extrusion of liquid metal from craters in a vacuum arc cathode spot," Journal of Applied Physics, 117(4).

[115] Fiflis, P., Christenson, M., Szott, M., Kalathiparambil, K., and Ruzic, D. N., 2016, "Free surface stability of liquid metal plasma facing components," Nuclear Fusion, 56(10), p. 106020.

[116] Coenen, J., Philipps, V., Brezinsek, S., Bazylev, B., Kreter, A., Hirai, T., Laengner, M., Tanabe, T., Ueda, Y., Samm, U., and the TEXTOR Team, 2011, "Analysis of tungsten melt-layer motion and splashing under tokamak conditions at textor," Nuclear Fusion, 51(8), jul, p. 083008.

[117] Krieger, K., Lunt, T., Dux, R., Janzer, A., Kallenbach, A., Müller, H., Neu, R., Pütterich, T., Rohde, V., Team, A. U., et al., 2011, "Induced tungsten melting events in

the divertor of ASDEX upgrade and their influence on plasma performance," Journal of nuclear materials, 415(1), pp. S297–S300.

[118] Lunz, D., and Howell, P. D., 2018, "Dynamics of a thin film driven by a moving pressure source," Physical Review Fluids, 3(11), Nov., p. 114801.

[119] Ren, J., Zuo, G. Z., Hu, J. S., Sun, Z., Yang, Q. X., Li, J. G., Zakharov, L. E., Xie, H., and Chen, Z. X., 2015, "A flowing liquid lithium limiter for the experimental advanced superconducting tokamak," Review of Scientific Instruments, 86(2), 02, p. 023504.

[120] Apicella, M., Apruzzese, G., Mazzitelli, G., Ridolfini, V. P., Alekseyev, A., Lazarev, V., Mirnov, S., and Zagórski, R., 2012, "Lithization of the FTU tokamak with a critical amount of lithium injection," Plasma Physics and Controlled Fusion, 54(3), p. 035001.

[121] Mirnov, S., Azizov, E., Evtikhin, V., Lazarev, V., Lyublinski, I., Vertkov, A., and Prokhorov, D. Y., 2006, "Experiments with lithium limiter on t-11m tokamak and applications of the lithium capillary-pore system in future fusion reactor devices," Plasma Physics and Controlled Fusion, 48(6), pp. 821–837.

[122] Zuo, G. Z., Hu, J. S., Maingi, R., Yang, Q. X., Sun, Z., Huang, M., Chen, Y., Yuan, X. L., Meng, X. C., Xu, W., Gentile, C., Carpe, A., Diallo, A., Lunsford, R., Mansfield, D., Osborne, T., Tritz, K., and Li, J. G., 2017, "Upgraded flowing liquid lithium limiter for improving li coverage uniformity and erosion resistance in east device," Review of Scientific Instruments, 88(12), 12, p. 123506.

[123] Li, C., Zuo, G., Maingi, R., Meng, X., Xu, W., Sun, Z., Qian, Y., Huang, M., Andruczyk, D., Tritz, K., et al., 2020, "Development of a new TZM substrate flowing liquid lithium limiter for high performance plasma discharge in EAST," Fusion Engineering and Design, 158, p. 111747.

[124] Li, C. L., Zuo, G. Z., Maingi, R., Tritz, K., Andruczyk, D., Zhang, B., Liang, R. R., Oliver, D., Sun, Z., Xu, W., Meng, X. C., Huang, M., Tang, Z. L., Gao, B. F., Yan, N., and Hu, J. S., 2022, "Evidence of vapor shielding effect on heat flux loaded on flowing liquid lithium limiter in east," Plasma Science and Technology, 24(9), p. 095104.

[125] Yang, J.-C., Liu, B.-Q., Huang, Y.-F., Lyu, Z., Dong, Q.-R., Pan, J.-H., and Ni, M.-J., 2023, "Experimental investigation of the flowing lithium limiter. part 1. the spreading characteristics of lithium on solid substrate without an external magnetic field," Fusion Engineering and Design, 189, p. 113489.

[126] Ellison, A. H., Klemm, R., Schwartz, A. M., Grubb, L., and Petrash, D. A., 1967, "Contact angles of mercury on various surfaces and the effect of temperature," Journal of Chemical and Engineering Data, 12(4), pp. 607–609.

[127] Hirsch, A., Dejace, L., Michaud, H. O., and Lacour, S. P., 2019, "Harnessing the rheological properties of liquid metals to shape soft electronic conductors for wearable applications," Accounts of Chemical Research, 52(3), pp. 534–544.

[128] Doudrick, K., Liu, S., Mutunga, E. M., Klein, K. L., Damle, V., Varanasi, K. K., and Rykaczewski, K., 2014, "Different shades of oxide: From nanoscale wetting mechanisms to contact printing of gallium-based liquid metals," Langmuir, 30(23), pp. 6867–6877.

[129] Dickey, M. D., 2014, "Emerging applications of liquid metals featuring surface oxides," ACS Applied Materials & Interfaces, 6(21), pp. 18369– 18379.

[130] Wang, M., Trlica, C., Khan, M., Dickey, M., and Adams, J., 2015, "A reconfigurable liquid metal antenna driven by electrochemically controlled capillarity," Journal of Applied Physics, 117(19).

[131] Xu, Q., Oudalov, N., Guo, Q., Jaeger, H. M., and Brown, E., 2012, "Effect of oxidation on the mechanical properties of liquid gallium and eutectic gallium-indium," Physics of Fluids, 24(6).

[132] Larsen, R. J., Dickey, M. D., Whitesides, G. M., and Weitz, D. A., 2009, "Viscoelastic properties of oxide-coated liquid metals," Journal of Rheology, 53(6), pp. 1305–1326.

[133] Handschuh-Wang, S., Chen, Y., Zhu, L., and Zhou, X., 2018, "Analysis and transformations of room-temperature liquid metal interfaces–a closer look through interfacial tension," ChemPhysChem, 19(13), pp. 1584–1592.

[134] Guo, R., Sun, X., Yuan, B., Wang, H., and Liu, J., 2019, "Magnetic liquid metal (Fe-EGaIn) based multifunctional electronics for remote self healing materials, degradable electronics, and thermal transfer printing," Advanced Science, 6(20), p. 1901478.

[135] Bilodeau, R. A., Zemlyanov, D. Y., and Kramer, R. K., 2017, "Liquid metal switches for environmentally responsive electronics.," Advanced Materials Interfaces, 4(5).

[136] Lu, H., Yun, G., Cole, T., Ouyang, Y., Ren, H., Shu, J., Zhang, Y., Zhang, S., Dickey, M. D., Li, W., et al., 2021, "Reversible underwater adhesion for soft robotic feet by leveraging electrochemically tunable liquid metal interfaces," ACS Applied Materials & Interfaces, 13(31), pp. 37904–37914.

[137] Joshipura, I. D., Ayers, H. R., Castillo, G. A., Ladd, C., Tabor, C. E., Adams, J. J., and Dickey, M. D., 2018, "Patterning and reversible actuation of liquid gallium alloys by preventing adhesion on rough surfaces," ACS applied materials & interfaces, 10(51), pp. 44686–44695.

[138] Ma, J., Bharambe, V. T., Persson, K. A., Bachmann, A. L., Joshipura, I. D., Kim, J., Oh, K. H., Patrick, J. F., Adams, J. J., and Dickey, M. D., 2020, "Metallophobic coatings to enable shape reconfigurable liquid metal inside 3d printed plastics," ACS Applied Materials & Interfaces, 13(11), pp. 12709–12718.

[139] Zhang, S., Wang, B., Jiang, J., Wu, K., Guo, C. F., and Wu, Z., 2019, "High-fidelity conformal printing of 3d liquid alloy circuits for soft electronics," ACS applied materials & interfaces, 11(7), pp. 7148–7156.

[140] Zhang, J., Yong, J., Zhang, C., Zhang, K., He, Y., Yang, Q., Hou, X., and Chen, F., 2020, "Liquid metal-based reconfigurable and repairable electronics designed by a femtosecond laser," ACS Applied Electronic Materials, 2(8), pp. 2685–2691.

[141] Lin, Q., Xing, C., Sui, R., Ci, W., and Xu, Y., 2019, "Effect of ultrasonic vibration on wetting of water/Cu, water/PTFE, E-GaIn/Cu and E-GaIn /graphite," Experimental Thermal and Fluid Science, 102, pp. 351–356.

[142] Dobosz, A., Daeneke, T., Zavabeti, A., Zhang, B. Y., Orrell-Trigg, R., Kalantar-Zadeh, K., Wójcik, A., Maziarz, W., and Gancarz, T., 2019, "Investigation of the surface of Ga-Sn-Zn eutectic alloy by the characterisation of oxide nanofilms obtained by the touch-printing method," Nanomaterials, 9(2), p. 235.

[143] Davis, E., and Ndao, S., 2018, "On the wetting states of low melting point metal galinstan® on silicon microstructured surfaces," Advanced Engineering Materials, 20(3), p. 1700829.

[144] Khan, M. R., Eaker, C. B., Bowden, E. F., and Dickey, M. D., 2014, "Giant and switchable surface activity of liquid metal via surface oxidation," Proceedings of the National Academy of Sciences, 111(39), pp. 14047–14051.

[145] Zhang, N., Shen, P., Cao, Y., Guo, R.-F., and Jiang, Q.-C., 2019, "Electrically induced spreading of egain on cu substrate in an alkali solution under wetting and non-wetting conditions," Applied Surface Science, 490, pp. 598–603.

[146] Tang, J., Zhao, X., Li, J., Guo, R., Zhou, Y., and Liu, J., 2017, "Gallium-based liquid metal amalgams: Transitional-state metallic mixtures (transm^{2}ixes) with enhanced and tunable electrical, thermal, and mechanical properties," ACS applied materials & interfaces, 9(41), pp. 35977– 35987.

[147] Guo, R., Wang, X., Chang, H., Yu, W., Liang, S., Rao, W., and Liu, J., 2018, "Ni-gain amalgams enabled rapid and customizable fabrication of wearable and wireless healthcare electronics," Advanced Engineering Materials, 20(10), p. 1800054.

[148] Guo, R., Yao, S., Sun, X., and Liu, J., 2019, "Semiliquid metal and adhesion-selection enabled rolling and transfer (smart) printing: A general method towards fast fabrication of flexible electronics," Science China Mater, 62(7), pp. 982–994.

[149] Ueki, Y., Nagai, K., Kunugi, T., Hirabayashi, M., Ara, K., Yonemoto, Y., and Hinoki, T., 2011, "Contact angle measurement of molten lead–lithium on silicon carbide surfaces," Fusion Engineering and Design, 86(9-11), pp. 2297– 2300.

[150] Pan, B. G., Wang, W. H., Chu, D. L., Yang, J. H., Mei, L. Q., Zhang, Q. H., Wang, P., and Wang, J., 2013, "Wetting angle measurement of liquid PbBi on RAFM steel surface based on ellipse fitting," Advanced Materials Research, 820, pp. 102–105.

[151] Saito, J.-I., and Monbernier, M., 2023, "Relationship between the contact angle of pure cu and its alloys owing to liquid Na and electronic states at the interface," Surfaces and Interfaces, 41, p. 103248.

[152] Ahmed, A., and Rangel, R., 2002, "Metal droplet deposition on non-flat surfaces: effect of substrate morphology," International Journal of Heat and Mass Transfer, 45(5), pp. 1077–1091.

[153] Solonenko, O., Gulyaev, I., and Smirnov, A., 2008, "Plasma processing and deposition of powdered metal oxides consisting of hollow spherical particles," Technical Physics Letters, 34, pp. 1050– 1052.

[154] Solonenko, O. P., Smirnov, A. V., and Gulyaev, I., 2008, "Spreading and solidification of hollow molten droplet under its impact onto substrate: computer simulation and experiment," In AIP Conference Proceedings, Vol. 982, American Institute of Physics, pp. 561–568.

[155] Kumar, A., and Gu, S., 2012, "Modelling impingement of hollow metal droplets onto a flat surface," International Journal of Heat and Fluid Flow, 37, pp. 189–195.

[156] Dhiman, R., and Chandra, S., 2005, "Freezing induced splashing during impact of molten metal droplets with high weber numbers," International Journal of Heat and Mass Transfer, 48(25-26), pp. 5625–5638.

[157] Ogura, T., Matsumoto, T., Miwa, S., Mori, M., and Hibiki, T., 2018, "Experimental study on molten metal spreading and deposition behaviors," Annals of Nuclear Energy, 118, pp. 353–362.

[158] Dou, Y., Luo, J., Qi, L., Lian, H., and Huang, J., 2021, "Drop-on-demand printing of recyclable circuits by partially embedding molten metal droplets in plastic substrates," Journal of Materials Processing Technology, 297, p. 117268.

[159] Huang, J., Qi, L., Luo, J., and Hou, X., 2021, "Insights into the impact and solidification of metal droplets in ground-based investigation of droplet deposition 3d printing under microgravity," Applied Thermal Engineering, 183, p. 116176.

[160] Yi, H., Qi, L., Luo, J., Zhang, D., Li, H., and Hou, X., 2018, "Effect of the surface morphology of solidified droplet on remelting between neighboring aluminum droplets," International Journal of Machine Tools and Manufacture, 130, pp. 1–11.

[161] Li, F., Hu, Y., Han, W., Fu, Y., Li, M., Li, C., and Hu, C., 2022, "Study of the process of metal droplets with high surface tension impinging on wall," Physics of Fluids, 34(11).

[162] Li, F., Hu, Y., Fu, Y., Li, G., Wei, R., Li, C., and Hu, C., 2023, "Dynamical behaviors of aluminum droplets impinging on horizontal and inclined surfaces," International Journal of Thermal Sciences, 186, p. 108146.

[163] Li, C., Han, S., Fu, Y., Li, F., Bai, W., and Hu, C., 2024, "Heat transfer process in the collision of high-temperature aluminum droplets with an inclined wall," Acta Astronautica, 215, pp. 168–177.

[164] Kim, B., Jang, J., You, I., Park, J., Shin, S., Jeon, G., Kim, J. K., and Jeong, U., 2015, "Interfacing liquid metals with stretchable metal conductors," ACS applied materials & interfaces, 7(15), pp. 7920–7926.

[165] Wu, Y.-h., Xing, S.-t., Zheng, R.-m., Liu, S.-q., Deng, Z.-f., Liu, H.-z., Wang, P.-p., and Liu, L., 2018, "Interface design for enhancing the wettability of liquid metal to polyacrylate for intrinsically soft electronics," Journal of Materials Chemistry C, 6(25), pp. 6755–6763.

[166] Zhao, R., Guo, R., Xu, X., and Liu, J., 2020, "A fast and cost-effective transfer printing of liquid metal inks for three-dimensional wiring in flexible electronics," ACS applied materials & interfaces, 12(32), pp. 36723–36730.

[167] Zhang, C., Yang, Q., Shan, C., Zhang, J., Yong, J., Fang, Y., Hou, X., and Chen, F., 2020, "Tuning a surface super-repellent to liquid metal by a femtosecond laser," RSC advances, 10(6), pp. 3301– 3306.

[168] Long, J., He, Z., Zhou, C., Xie, X., Cao, Z., Zhou, P., Zhu, Y., Hong, W., and Zhou, Z., 2018, "Hierarchical micro-and nanostructures induced by nanosecond laser on copper for superhydrophobicity, ultralow water adhesion and frost resistance," Materials & Design, 155, pp. 185–193.

[169] Chen, L., Wang, X., Yang, T., Ping, H., Bennett, P., Zheng, Z., Yang, Q., Perrie, W., Edwardson, S. P., Dearden, G., et al., 2018, "Superhydrophobic micro-nano structures on

silicone rubber by nanosecond laser processing," Journal of Physics D: Applied Physics, 51(44), p. 445301.

[170] Long, J., Weng, Q., Hong, W., Cao, Z., Zhou, P., and Xie, X., 2019, "Fast water flow in laser micromachined microgrooves with nonuniform surface wettability," Experimental Thermal and Fluid Science, 103, pp. 9–17.

[171] Fu, J., Liang, H., Zhang, J., Wang, Y., Liu, Y., Zhang, Z., and Lin, X., 2017, "Enhanced optical absorbance and fabrication of periodic arrays on nickel surface using nanosecond laser," Optics Communications, 389, pp. 170–175.

[172] Tagawa, T., 2007, "Numerical simulation of liquid metal free-surface flows in the presence of a uniform static magnetic field," ISIJ international, 47(4), pp. 574–581.

[173] Yang, J.-C., Qi, T.-Y., Han, T.-Y., Zhang, J., and Ni, M.-J., 2018, "Elliptical spreading characteristics of a liquid metal droplet impact on a glass surface under a horizontal magnetic field," Physics of Fluids, 30(1).

[174] Zhou, J., Cheng, Z., Tang, Y., and Yang, J., 2024, "Investigation of the spreading of a liquid metal droplet under a vertical magnetic field," Physics of Fluids, 36(4).

[175] Han, T.-Y., Yang, J.-C., Zhang, J., and Ni, M.-J., 2018, "Three-dimensional numerical simulation on the spreading characteristics of a liquid metal droplet in a horizontal magnetic field," Numerical Heat Transfer, Part A: Applications, 74(12), pp. 1786–1803.

[176] Meng, X., Wang, Z.-H., Cai Z.-Y., and Zhang, D.-K., 2022, "Experimental study of gallium droplet impacting on solid wall under the strong magnetic field," Chinese Journal of Theoretical and Applied Mechanics, 54(2), pp. 396–404.

[177] Han, T.-Y., Zhang, J., and Ni, M.-J., 2024, "Maximum spreading of a liquid metal droplet under a horizontal magnetic field," Physical Review Fluids, 9(10), p. 103703.

[178] Sun, S.-R., Zhang, J., and Ni, M.-J., 2022, "Solidification of liquid metal droplet during impact in the presence of vertical magnetic field," Physics of Fluids, 34(5).

[179] Li, X.-Y, Yang, Y.-H., Chen, H., and Xu, J.-J., 2003, "Experiment study of the coupling effect between film boiling heat transfer and evaporation drag around a high-temperature particle in cold liquid during coarse mixing stage of vapor explosion," Nuclear Power Engineering, 24.

[180] Zhang, J., Hu, Z., Li, X., Kuang B., Yang, Y., and Borisenko, D., 2004, "Experimental study on the boiling movement process of the high-temperature particles falling into the cold liquid," Atomic Energy Science and Technology, 38.

[181] Li, L., Li, H., and Chen, T., 2008, "Experimental investigation on the moving characteristics of molten metal droplets impacting coolant," Experimental Thermal and Fluid Science, 32(4), pp. 962– 972.

[182] Wang, J.-J., Zhang, J., Ni, M.-J., and Moreau, R., 2014, "Numerical study of single droplet impact onto liquid metal film under a uniform magnetic field," Physics of Fluids, 26(12).

[183] Hadj-Achour, M., Rimbert, N., Gradeck, M., and Meignen, R., 2021, "Fragmentation of a liquid metal droplet falling in a water pool," Physics of Fluids, 33(10).

[184] Li, H., Mei, S., Wang, L., Gao, Y., and Liu, J., 2014, "Splashing phenomena of room temperature liquid metal droplet striking on the pool of the same liquid under ambient air environment," International Journal of Heat and Fluid Flow, 47, pp. 1–8.

[185] Ren, D.-W., Wu, S., Yang, J.-C., and Ni, M.-J., 2020, "Investigation of liquid metal drop impingement on a liquid metal surface under the influence of a horizontal magnetic field," Physics of Fluids, 32(5).

[186] Menchaca-Rocha, A., Huidobro, F., MartinezDavalos, A., Michaelian, K., Perez, A., Rodriguez, V., and Carjan, N., 1997, "Coalescence and fragmentation of colliding mercury drops," Journal of Fluid Mechanics, 346, pp. 291–318.

[187] Xia, S.-y., and Hu, C.-b., 2015, "Numerical investigation of head-on binary collision of alumina droplets," Journal of Propulsion and Power, 31(1), pp. 416–428.

[188] Hu, C., Xia, S., Li, C., and Wu, G., 2017, "Three dimensional numerical investigation and modeling of binary alumina droplet collisions," International Journal of Heat and Mass Transfer, 113, pp. 569– 588.

[189] Jia, X., Yang, J.-C., Zhang, J., and Ni, M.-J., 2019, "An experimental investigation on the collision outcomes of binary liquid metal droplets," International Journal of Multiphase Flow, 116, pp. 80–90.

[190] Jia, X., Yang, J.-C., Zhang, J., Chen, L., and Ni, M.-J., 2021, "Collision dynamics of binary liquid metal droplets under horizontal magnetic field," Physical Review Fluids, 6(10), p. 103702.

[191] Duineveld, P., 1995, "The rise velocity and shape of bubbles in pure water at high reynolds number," Journal of Fluid Mechanics, 292, pp. 325–332.

[192] Lunde, K., and Perkins, R., 1997, "Observations on wakes behind spheroidal bubbles and particles," In ASME FED Summer Meeting, Vancouver, Canada, Paper FEDSM, pp. 97–3530.

[193] Brucker, C., 1999, "Structure and dynamics of the¨ wake of bubbles and its relevance for bubble interaction," Physics of Fluids (1994-present), 11(7), pp. 1781–1796.

[194] Ellingsen, K., and Risso, F., 2001, "On the rise of an ellipsoidal bubble in water: oscillatory paths and liquid-induced velocity," Journal of Fluid Mechanics, 440, pp. 235–268.

[195] Zhang, J., and Ni, M.-J., 2017, "What happens to the vortex structures when the rising bubble transits from zigzag to spiral?," Journal of Fluid Mechanics, 828, pp. 353–373.

[196] De Vries, A., Biesheuvel, A., and Van Wijngaarden, L., 2002, "Notes on the path and wake of a gas bubble rising in pure water," International Journal of Multiphase Flow, 28(11), pp. 1823–1835.

[197] Veldhuis, C., Biesheuvel, A., and Van Wijngaarden, L., 2008, "Shape oscillations on bubbles rising in clean and in tap water," Physics of Fluids (1994-present), 20(4), p. 040705.

[198] Zenit, R., and Magnaudet, J., 2009, "Measurements of the streamwise vorticity in the wake of an oscillating bubble," International Journal of Multiphase Flow, 35(2), pp. 195–203.

[199] Sanada, T., Shirota, M., and Watanabe, M., 2007, "Bubble wake visualization by using photochromic dye," Chemical Engineering Science, 62(24), pp. 7264–7273.

[200] Zenit, R., and Magnaudet, J., 2008, "Path instability of rising spheroidal air bubbles: a shape controlled process," Physics of Fluids, 20(6).

[201] Veldhuis, C., Biesheuvel, A., and Van Wijngaarden, L., 2008, "Shape oscillations on bubbles rising in clean and in tap water," Physics of fluids, 20(4).

[202] Pesci, C., Weiner, A., Marschall, H., and Bothe, D., 2018, "Computational analysis of single rising bubbles influenced by soluble surfactant," Journal of Fluid Mechanics, 856, pp. 709–763.

[203] Mori, Y., Hijikata, K., and Kuriyama, I., 1977, "Experimental study of bubble motion in mercury with and without a magnetic field," Journal of Heat Transfer, 99(3), pp. 404–410.

[204] Iguchi, M., Nakatani, T., and Kawabata, H., 1997, "Development of a multineedle electroresistivity probe for measuring bubble characteristics in molten metal baths," Metallurgical and Materials Transactions B, 28, pp. 409–416.

[205] Takeda, Y., 2012, Ultrasonic Doppler velocity profiler for fluid flow, Vol. 101 Springer Science & Business Media.

[206] Wang, Z., Wang, S., Meng, X., and Ni, M., 2017, "UDV measurements of single bubble rising in a liquid metal galinstan with a transverse magnetic field," International Journal of Multiphase Flow, 94, pp. 201–208.

[207] Vogt, T., Boden, S., Andruszkiewicz, A., Eckert, K., Eckert, S., and Gerbeth, G., 2015, "Detection of gas entrainment into liquid metals," Nuclear Engineering and Design, 294, pp. 16–23.

[208] Timmel, K., Shevchenko, N., Roder, M., Anderhu-¨ ber, M., Gardin, P., Eckert, S., and Gerbeth, G., 2015, "Visualization of liquid metal two-phase flows in a physical model of the continuous casting process of steel," Metallurgical and Materials Transactions B, 46, pp. 700–710.

[209] Keplinger, O., Shevchenko, N., and Eckert, S., 2017, "Validation of x-ray radiography for characterization of gas bubbles in liquid metals," In IOP Conference Series: Materials Science and Engineering, Vol. 228, IOP Publishing, p. 012009.

[210] Saito, Y., Mishima, K., Tobita, Y., Suzuki, T., Matsubayashi, M., Lim, I., and Cha, J., 2005, "Application of high frame-rate neutron radiography to liquid-metal two-phase flow research," Nuclear Instruments and Methods in Physics Research Section A: Accelerators, Spectrometers, Detectors and Associated Equipment, 542(1-3), pp. 168–174.

[211] Gou, H., Lyu, Z., Ni, M.-J., and Yao, Z., 2024, "Motion characteristics of a single bubble in liquid metal under a streamwise magnetic field," Physics of Fluids, 36(9).

[212] Murakawa, H., Maeda, S., and Eckert, S., 2024, "Effects of a horizontal magnetic field on the crosssectional distribution of gas bubbles chain rising in a gallium alloy," International Journal of Multiphase Flow, 170, p. 104649.

[213] Fröhlich, J., Schwarz, S., Heitkam, S., Santarelli, C., Zhang, C., Vogt, T., Boden, S., Andruszkiewicz, A., Eckert, K., Odenbach, S., et al., 2013, "Influence of magnetic fields on the behavior of bubbles in liquid metals," The European Physical Journal Special Topics, 220, pp. 167–183.

[214] Zheng, X.-L., Pan, J.-H., and Ni, M.-J., 2023, "Linear global stability of a flow past a sphere under a streamwise magnetic field," Journal of Fluid Mechanics, 970, p. A16.

[215] Strumpf, E., 2017, "Experimental study on rise velocities of single bubbles in liquid metal under the influence of strong horizontal magnetic fields in a flat vessel," International Journal of Multiphase Flow, 97, pp. 168–185.

[216] Zhang, J., Ni, M.-J., and Moreau, R., 2016, "Rising motion of a single bubble through a liquid metal in the presence of a horizontal magnetic field," Physics of Fluids, 28(3).

[217] Zhang, J., Sahu, K. C., and Ni, M.-J., 2021, "Transition of bubble motion from spiralling to zigzagging: A wake-controlled mechanism with a transverse magnetic field," International Journal of Multiphase Flow, 136, p. 103551.

[218] Moreau, R. J., 2013, Magnetohydrodynamics, Vol. 3 Springer Science & Business Media.

[219] Davidson, P. A., and Thess, A., 2002, Magnetohydrodynamics, Vol. 418 Springer Science & Business Media.

[220] Miao, X., Lucas, D., Ren, Z., Eckert, S., and Gerbeth, G., 2013, "Numerical modeling of bubble driven liquid metal flows with external static magnetic field," International Journal of Multiphase Flow, 48, pp. 32–45.